New solar-sail orbits for polar observation of the earth and moon

Losada, Fernando Gámez; Heiligers, Jeannette

DOI
10.2514/1.G005955

Publication date
2021

Document Version
Accepted author manuscript

Published in
Journal of Guidance, Control, and Dynamics

New solar-sail orbits for polar observation of the Earth and Moon *

Fernando Gámez Losada † and Jeannette Heiligers ‡
Delft University of Technology, Delft, The Netherlands, 2629 HS

In this paper, a new family of solar-sail periodic orbits with adequate properties for polar observation of the Earth and Moon is developed under the simplified but non-autonomous dynamics of the solar-sail augmented Earth-Moon circular-restricted three-body problem. The novel orbits, termed distant-circular orbits, are found through differential correction and continuation and employ a simple Sun-facing steering law for the solar sail. A basic coverage analysis shows that one of the distant-circular orbits is capable of providing continuous coverage of both the Earth's and lunar north (or south) poles with just a single sailcraft at a minimum elevation angle of 14 deg and an average range of six Earth-Moon distances. Moreover, simple transfer trajectories between orbits of the family are found, so that the sailcraft can switch between observing the northern and southern latitudes of the Earth and Moon during a single mission. Subsequently, using multiple-shooting differential correction, all results are migrated to a higher-fidelity dynamical framework which considers, among others, the eccentricity of the Moon's orbit. The perturbations cause the periodicity of the orbits to break, turning them into seemingly quasi-periodic orbits, but it is shown that the coverage capabilities are maintained. Finally, an active control strategy is developed to counteract part of the perturbing effects such that, by appropriately steering the sail, the apparent quasi-periodicity of the orbits is enhanced and the deviation from the unperturbed orbits is reduced.

I. Introduction

Over recent years, solar-sail propulsion has developed from a theoretical concept to a flight proven form of low-thrust propulsion. In 2010, JAXA was the first to prove the viability of solar sailing with its sailcraft IKAROS [1]. Also that year, NASA launched NanoSail-D2, a CubeSat technology demonstration mission that successfully validated the concept of solar-sail propulsion for small satellite platforms [2]. In later years, the Planetary Society launched LightSail-1 (2015) and LightSail-2 (2019), the last one effectively using the sail to raise the apogee of its orbit around Earth [3, 4]. With

*The content of this paper was presented in the AAS/AIAA Astrodynamics Specialist Conference which was held August 9-13, 2020, virtually, and with an AIAA Paper Number of AAS 20-437.

†Graduate Student, Department of Astrodynamics and Space Missions, Faculty of Aerospace Engineering, fer202122@gmail.com

‡Assistant Professor, Department of Astrodynamics and Space Missions, Faculty of Aerospace Engineering, M.J.Heiligers@tudelft.nl

NASA's NEA Scout [5] and Solar Cruiser [6] missions on the horizon, it seems that solar-sail technology will continue to mature and enable many scientific missions otherwise unachievable with conventional propulsion [7].

A solar sail can be considered a large thin mirror-like surface that reflects sunlight. The solar photons exchange their momentum upon interaction with the sail membrane, which induces a small thrust directed mainly perpendicular to the surface of the sail [8]. Although the solar-sail induced acceleration is almost negligible in magnitude, this new form of low-thrust space propulsion has been theoretically proven to outperform conventional propulsion systems reliant on an on-board reaction mass for a range of high-energy and long-duration missions [7]. For instance, solar sails can be used to accelerate a spacecraft to the outer rim of the Solar System [9] or to increase the energy of an impactor aimed to deviate a threatening asteroid [10]. Since solar-sail propulsion does not require propellant, the only constraint on the duration of the mission is the lifetime of the sail film as it degrades in the harsh space environment [11].

The bulk of research related to the orbital dynamics and mission design of solar-sail propelled spacecraft focuses on the Sun-Earth system. One example is the pole-sitter concept that places a solar sail around the polar axis of the Earth so that one sailcraft is capable of providing continuous coverage of the polar regions [12, 13]. The pole-sitter concept is designed in the Sun-Earth circular restricted three-body problem, augmented with the solar-sail acceleration. As an alternative, several studies have shown the potential of solar-sail periodic orbits in the Earth-Moon system for coverage of the high-latitudes of either the Earth or Moon [14–17]. Despite the non-autonomous nature of the solar-sail augmented Earth-Moon system, rich families of solar-sail periodic orbits exist. In [14], the authors extend a range of traditional families of libration-point orbits with solar-sail propulsion whose applications are further investigated in [15], where different constellations of two sailcrafts in so-called clover-shaped orbits and vertical Lyapunov orbits are designed for continuous observation of the high-latitudes of the Earth and Moon. Finally, [16] and [17] present an extensive numerical study into solar-sail orbits specifically for lunar south pole coverage using only a single sailcraft. In this paper, we develop a new family of solar-sail displaced orbits, termed distant-circular (DC) orbits, for the purpose of polar coverage of the Earth and Moon. Similar to the pole-sitter concept and the work in [16] and [17], the DC orbits require only one sailcraft for continuous coverage of either the Earth or lunar pole. However, compared to the pole-sitter concept, the DC orbits allow the spacecraft to be positioned closer to the Earth and Moon, hence improving the spatial resolution of the observations; compared to the orbits proposed in [16] and [17], the DC orbits present a more realistic mission scenario as they rely on much more near-term solar-sail technology. Requiring only one sailcraft is the main advantage of DC orbits compared to the clover-shaped and vertical Lypaunov orbit constellations proposed in [15], though at greater orbital distances. The DC orbits therefore presents a new trade-off solution in terms of spatial resolution and number of spacecraft required, sitting "midway" of the pole-sitter and the constellations in [15].

Like all mission concepts presented in [12, 13, 15–17], the DC orbits only allow the observation of one of the poles of the Earth and Moon at any time. To increase the mission scientific return, we investigate novel transfers between DC orbits above and below the Earth-Moon orbital plane. Such transfers give a sole sailcraft the capability of observing

both the northern and southern latitudes of the Earth and/or Moon during a single mission.

An additional novel contribution of this paper comes in the form of an active control strategy to counteract a range of perturbations not considered in the circular restricted three-body problem (CR3BP) without the need for propulsion methods other than the solar sail. Most of the solar-sail periodic orbits found in the solar-sail augmented Earth-Moon three-body system rely on four fundamental simplifications that assume the following to be zero: the eccentricity of the Moon's orbit, the plane offset between the Earth-Moon orbital plane and the ecliptic, the Sun's gravitational perturbation, and the heliocentric eccentricity of the orbit of the Earth-Moon system (EMS)-barycenter [15]. When relaxed, these simplifications cause perturbations that impair periodicity and often induce significant deviations from the designed orbits. In the works mentioned above, the authors repeatedly suggest the necessity for an active control strategy to palliate these effects especially considering the inherent linear instability of all developed orbits. In this paper, we develop such an active control strategy in the form of a weight-optimized multiple shooting algorithm.

The remainder of this paper is organized as follows: first, Section II summarizes the low- and high-fidelity dynamical models used throughout the work. Subsequently, Section III presents the newly developed family of distant-circular orbits in the low-fidelity dynamical framework (the reference orbits) together with a discussion on their performance in terms of coverage of the Earth's and lunar poles. Then, Section IV develops a multiple-shooter differential correction scheme to modify the reference orbits so that they hold under the higher fidelity dynamics but using the reference control. Section V repeats the latter process but allows for active control to reduce the deviations from the reference orbits. Finally, Section VI presents feasible transfers between distant-circular orbits above and below the Earth-Moon plane to further increase the scientific return of this new mission concept.

II. Dynamical System

Throughout this section the parameters and notation in Table 1 are used to describe the geometry and motion of the Moon with respect to the Earth and that of the EMS-barycenter around the Sun. Note that the values in Table 1 are the exact values used in the computations. In this study, we assume that the Moon follows an unperturbed ellipse described by the mean values a, e, n and i_{off}, which restricts the validity of the analyses in this paper to a time-scale of approximately one year. The next subsections present the three dynamical frameworks used to model the EMS and the equations of motion (EoM) of the solar sail.

A. Dynamical Frameworks

Throughout this work we employ three dynamical frameworks to describe the motion of the solar sail. They are all based on the solar-sail CR3BP but are of increasing fidelity by adding different perturbative effects. Figure 1a sorts the dynamical frameworks from simple to more complex from left to right and gives the dynamical parameters that are active in each case. As a starting point, the simplest mathematical representation that captures the essence of the

Table 1 Dynamical parameters of the EMS used in the computations [18].

Parameter	Value
Dimensionless mass, Moon, μ	0.012 150 585 6
Dimensionless mass, Sun, μ_4	3.2893×10^5
Semi-major axis, Moon, a	$0.384\,401 \times 10^6$ km
Eccentricity, Moon, e	0.0549
Mean motion, Moon, n	$2.665\,293\,292\,445\,35 \times 10^{-6}$ rad s^{-1}
Inclination, Moon, i_{off}	5.145 deg
Semi-major axis, barycenter, a_h	$149.597\,870\,7 \times 10^6$ km
Eccentricity, barycenter, e_h	0.01671022
Mean motion, barycenter, n_h	$1.993\,639\,382\,749\,122 \times 10^{-7}$ rad s^{-1}

dynamics is the solar-sail CR3BP, where the Earth and Moon revolve around their common center of mass in circular orbits and the gravitational influence of the sailcraft on the two main bodies is neglected; this approximation discards all external dynamical effects [8]. Moreover, the Sun's apparent motion is reduced to a clockwise circular orbit around the barycenter that lies within the Earth-Moon orbital plane and has a radius a_h and a dimensionless angular velocity of $\Omega_4 = 1 - n_h/n = 0.9252$ (see Fig. 1b). The next step on the complexity scale is the solar-sail Sun-gravity circular restricted three-body problem (SgC) (see again Fig. 1a). Maintaining all the assumptions of the solar-sail CR3BP, the Sun's gravitational attraction (μ_4) is added to the dynamics as a fourth-body acceleration on the sailcraft. Next, the introduction of the eccentricity of the Moon's orbit (e) yields the solar-sail Sun-gravity elliptical restricted three-body problem (SgE). In this framework, the circular motion of the primaries is substituted by Keplerian ellipses, which are entirely described by the two-body problem formulation. Note that, in this dynamical model, the Sun's apparent angular velocity becomes time-dependent since the rotation of the EMS in no longer constant. Finally, the high-fidelity (HF) framework adds two further dynamical effects to the SgE: the eccentricity of the EMS orbit around the Sun (e_h), and the plane offset between the EMS orbital plane and the ecliptic plane (i_{off}). Despite the increased fidelity, this framework still assumes that the orbit of the Moon is a non-perturbed Keplerian orbit.

In addition to the parameters considered in each dynamical framework, Fig. 1a also provides the name convention for the orbits that hold under each particular model. The orbits in the SgC framework will act as *reference*. The *e-corrected* orbits in the SgE framework are only corrected for the eccentricity of the orbit of the Moon, using the solar-sail control law of the reference orbits. The *natural* orbits of the HF framework also use the control law of the reference orbits, whereas the *controlled* orbits employ active control to counter the perturbations. Finally, the *controlled* orbits are further divided into two categories, depending on how the control law is calculated (see Section V for further details).

No matter which dynamical framework is used, all trajectory propagations start from the same initial state (see Fig. 2a). At the initial time ($t = 0$), the Sun is positioned along the Earth-Moon line with the Earth between the Sun and Moon, the Earth is at perihelion and the Moon at perigee. Furthermore, for the HF model, the EMS plane is tilted with respect to the ecliptic at an angle i_{off} so that the Earth is above the ecliptic at the initial state, whereas the Moon is

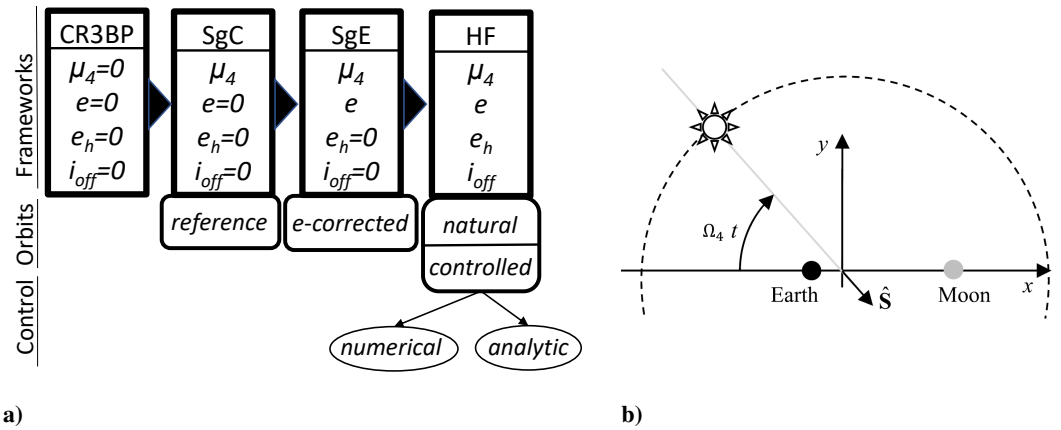

a) b)

Fig. 1 Schematics of a) the dynamical frameworks and orbit types considered in this paper, and b) the Sun's apparent motion around the EMS-barycenter (adapted from [15]).

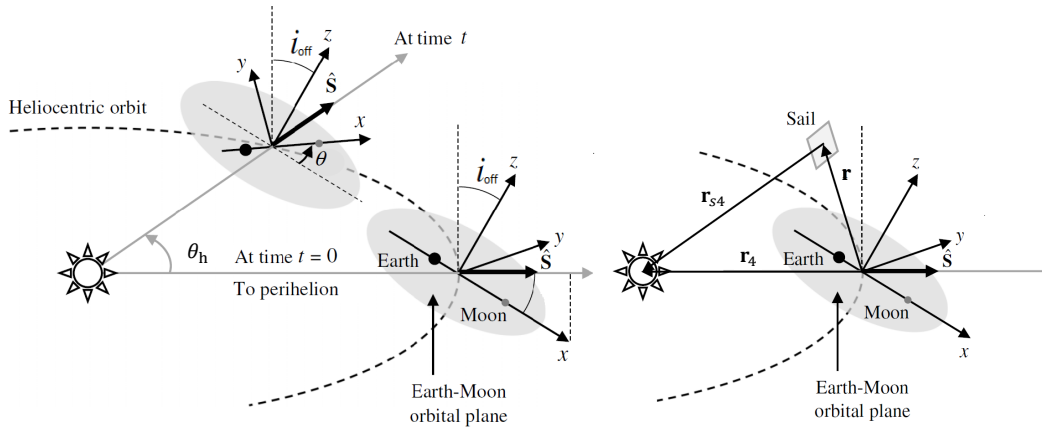

a) b)

Fig. 2 Schematics of a) the initial and general configuration of the EMS, and b) the vectors that define the Sun's gravitational perturbation (extracted from [15]).

below the ecliptic (see Fig. 2a).

B. Equations of Motion

The differential equations governing the motion of the solar sail are formulated in the HF dynamical framework. By setting certain parameters to zero (see Fig. 1a) it is possible to switch to all the other frameworks discussed in the previous subsection. The following formulation is based on the work in [15] with one major difference: the eccentricity of the Moon is not included via pulsating coordinates commonly employed in the elliptical restricted three-body problem, where an independent variable change from time to true anomaly is performed so that the EoM adopt a more manageable form [19]. Even though the EoM in pulsating coordinates are more compact, the physical meaning of the velocities and accelerations is lost. Hence, the non-uniformly co-rotating reference frame $C(\hat{\boldsymbol{x}}, \hat{\boldsymbol{y}}, \hat{\boldsymbol{z}})$, centered in the EMS-barycenter (see Fig. 3a) is used to express the solar-sail state vector and its derivatives as a function of time. The $\hat{\boldsymbol{x}}$-axis coincides

with the line connecting the two primaries in their elliptical motion around the barycenter and points towards the Moon, the $\hat{z}$-axis is aligned with the angular momentum vector of the EMS and the $\hat{y}$-axis completes the right-handed triad. Traditional canonical units are used to scale the variables so that the inverse of the mean motion of the Moon's orbit (n) is the unit of time, the semi-major axis of the Moon's orbit (a) is the unit of length and the total mass of the EMS is the unit of mass. In reference frame C, the solar-sail dynamics are described by:

$$\frac{d\boldsymbol{X}}{d\,t} = \boldsymbol{f}(\boldsymbol{X}, \boldsymbol{u}, t) \tag{1}$$

where $X = [\,\boldsymbol{r} \quad \dot{\boldsymbol{r}}\,]^{\intercal}$ is the solar-sail state vector (position and velocity), $\boldsymbol{f} = [\,\dot{\boldsymbol{r}} \quad \ddot{\boldsymbol{r}}\,]^{\intercal}$ its derivative with respect to time (velocity and acceleration) and $\boldsymbol{u}$ represents the control law.

The solar-sail position vector expressed in C is $\boldsymbol{r} = [\,x \quad y \quad z\,]^{\intercal}$, and its second-order derivative with respect to time equals:

$$\ddot{\boldsymbol{r}} = \boldsymbol{a_{rot}} + \boldsymbol{a_E} + \boldsymbol{a_M} + \boldsymbol{a_4} + \boldsymbol{a_s} \tag{2}$$

where $\boldsymbol{a_{rot}}$ represents the rotational term associated with the non-uniform rotation of C; $\boldsymbol{a_E}$ and $\boldsymbol{a_M}$ the gravitational acceleration induced by the Earth and Moon, respectively; $\boldsymbol{a_4}$ the Sun's gravitational perturbation; and $\boldsymbol{a_s}$ the solar-sail acceleration due to the solar radiation pressure acting on the sail. Hereafter, we elaborate on the precise formulation of each of these terms.

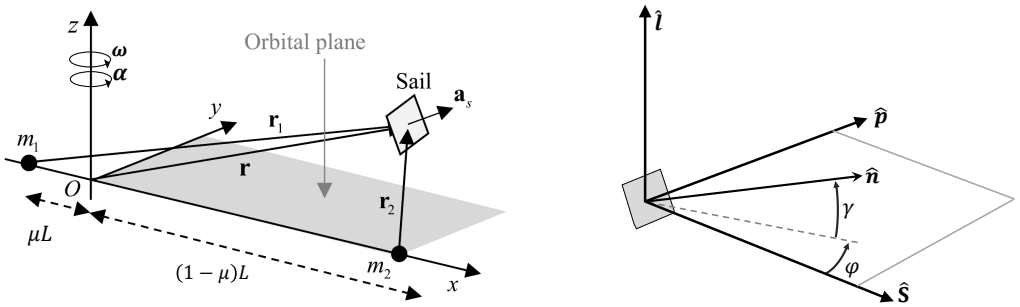

Fig. 3 Schematics of a) the reference frame $C(\hat{x}, \hat{y}, \hat{z})$ (adapted from [15]), and b) the reference frame $S(\hat{S}, \hat{p}, \hat{l})$ with a definition of the attitude angles of the solar sail.

1. Rotational Term

When expanded, the rotational term reads as:

$$\boldsymbol{a_{rot}} = -\left(2\boldsymbol{\omega} \times \dot{\boldsymbol{r}} + \boldsymbol{\alpha} \times \boldsymbol{r} + \boldsymbol{\omega} \times (\boldsymbol{\omega} \times \boldsymbol{r})\right) \tag{3}$$

where $\boldsymbol{\omega} = \dot{\theta}\hat{\boldsymbol{z}}$ and $\boldsymbol{\alpha} = \ddot{\theta}\hat{\boldsymbol{z}}$ represent the vectors of angular velocity and angular acceleration of C. The magnitudes of these vectors are equal to the first-and second-order derivatives of the Moon's true anomaly (θ) when viewed from Earth. Referring to the two-body problem formulation, these derivatives can be written in terms of θ as follows [20]:

$$\dot{\theta} = \frac{(1 + e\cos\theta)^2}{(1 - e^2)^{3/2}} \tag{4}$$

$$\ddot{\theta} = -2\,\dot{\theta}^2 \frac{e\ \sin\theta}{1 + e\ \cos\theta} \tag{5}$$

where e is the eccentricity of the Moon (see Table 1).

2. Gravitational Acceleration Induced by the Earth and Moon

The Earth and Moon gravitational terms expand as:

$$\boldsymbol{a_E} = -(1 - \mu)\frac{\boldsymbol{r_1}}{r_1^3} \tag{6}$$

$$\boldsymbol{a_M} = -\mu\frac{\boldsymbol{r_2}}{r_2^3}\,. \tag{7}$$

where μ is the dimensionless mass of the Moon (see Table 1). Note that the position vectors of the sailcraft relative to the primaries $\boldsymbol{r_1} = [\,x + \mu L \quad y \quad z\,]^\intercal$ and $\boldsymbol{r_2} = [\,x - (1 - \mu L) \quad y \quad z\,]^\intercal$ contain the term L, which accounts for the varying distance between the primaries on their elliptical orbits around the barycenter [19]:

$$L = \frac{1 - e^2}{1 + e\cos\theta}\,. \tag{8}$$

Hence, the primaries seem to "wobble" around an equilibrium position along the $\hat{\boldsymbol{x}}$-axis as time progresses. In accordance with the chosen initial condition (see Fig. 2a), L is minimum at the initial time.

3. Gravitational Acceleration Induced by the Sun

The gravitational effect of the Sun is introduced as a fourth-body acceleration [15]:

$$\boldsymbol{a_4} = \mu_4\left(\frac{\boldsymbol{r_{s4}}}{r_{s4}^3} - \frac{\boldsymbol{r_4}}{r_4^3}\right) \tag{9}$$

where μ_4 is the dimensionless mass of the Sun (see Table 1), $\boldsymbol{r_4}$ is the Earth-Sun vector and $\boldsymbol{r_{s4}} = \boldsymbol{r_4} - \boldsymbol{r}$ is the sail-Sun vector (see Fig. 2b). To define $\boldsymbol{r_4}$, we introduce the unit vector $\hat{\boldsymbol{S}}$, which is aligned with the direction of sunlight (see

Figs. 1b and 2). The following sequence of rotations yields the Cartesian coordinates of $\hat{\boldsymbol{S}}$ in the reference frame C [15]:

$$\hat{\boldsymbol{S}} = \mathrm{R_z}(-\theta)\mathrm{R_y}(-i_{off})\mathrm{R_z}(\theta_h)\begin{bmatrix}1\\0\\0\end{bmatrix} \tag{10}$$

where $\mathrm{R_z}(\theta_h)$ accounts for the motion of the barycenter around the Sun, $\mathrm{R_y}(-i_{off})$ for the offset between the EMS and ecliptic planes, and $\mathrm{R_z}(-\theta)$ for the rotation of C within the orbital plane of the EMS (see Fig. 2a). Then, $\boldsymbol{r_4}$ can be expressed as [15]:

$$\boldsymbol{r_4} = -\frac{a_h}{a}\frac{1-e_h^2}{1+e_h\cos\theta_h}\hat{\boldsymbol{S}} \tag{11}$$

where a_h, e_h and θ_h are the semi-major axis, eccentricity and true anomaly of the barycenter's heliocentric orbit (see Table 1).

4. Solar-Sail Acceleration

In this study, we neglect all optical and geometrical imperfections of the sail membrane and adopt the ideal solar-sail acceleration model. The ideal model assumes pure specular reflection of the incoming photons, causing the solar-sail acceleration vector to act perpendicular to the sail [15]:

$$\boldsymbol{a_s} = a_0\left(\frac{a_h}{r_4}\right)^2\left(\hat{\boldsymbol{S}}\cdot\hat{\boldsymbol{n}}\right)^2\hat{\boldsymbol{n}} \tag{12}$$

where a_0 is the solar-sail characteristic acceleration and $\hat{\boldsymbol{n}}$ is the unit vector normal to the sail membrane. The quantity a_0 is defined as the magnitude of the solar-sail acceleration when the sail is placed perpendicular to the incoming sunlight (*i.e.*, $\hat{\boldsymbol{S}}$ and $\hat{\boldsymbol{n}}$ are parallel) at one astronomical unit from the Sun. Hence, a_0 depends on both the solar radiation pressure at one astronomical unit, the effective area of the sail membrane and the spacecraft mass [8]. For this study we assume a feasible near-term value for a_0 of $0.3\,\mathrm{mm/s^2}$ (*i.e.*, approximately 0.1 in dimensionless units) for the generation of the reference orbits [7, 21]. In Eq. (12), the term $(a_h/r_4)^2$ scales a_0 to account for variations in the heliocentric radial distance due to e_h. This scaling is required because, in the HF framework, the distance between the Sun and the EMS-barycenter is no longer constant at one astronomical unit, which changes the solar radiation pressure experienced at the EMS-barycenter. Finally, note that Eq. (12) neglects the variation in $\boldsymbol{a_s}$ due to the motion of the solar sail within the EMS, i.e., we assume that the solar radiation pressure is constant throughout the EMS.

In this paper, the solar-sail acceleration is controlled by two angles (that uniquely define the orientation of $\hat{\boldsymbol{n}}$) and by a variation in a_0 around its reference value of $0.3\,\mathrm{mm/s^2}$. We can then write the control law as $\boldsymbol{u} = [\,\gamma \quad \varphi \quad a_0\,]^\intercal$, where the angles γ and φ are defined in Fig. 3b. The angles are bounded to the interval $[-90, 90]$ deg, such that the

back of the sail membrane is never exposed to the Sun. Also note that by defining the bounds on the angles as such, ambiguity in the angles are avoided. The orthogonal reference frame employed to define γ and φ (see Fig. 3b), $S(\hat{\boldsymbol{S}}, \hat{\boldsymbol{p}}, \hat{\boldsymbol{l}})$, is centered at the solar sail, where the $\hat{\boldsymbol{S}}$-axis matches the Sun-sail line (i.e., the $\hat{\boldsymbol{S}}$ vector), the $\hat{\boldsymbol{p}}$-axis is contained in the ecliptic plane and the $\hat{\boldsymbol{l}}$-axis is aligned with the ecliptic north pole. To better understand the possible orientations of $\boldsymbol{a_s}$ within frame S, it is useful to introduce the concept of the acceleration bubble. The acceleration bubble is an imaginary bubble-shaped surface in the frame S that contains all feasible $\boldsymbol{a_s}$ vectors [22]. Figure 4a depicts an schematic of this acceleration bubble. The shown vector $\boldsymbol{a_s}$ in Fig. 4a is the largest (in magnitude) achievable solar-sail acceleration vector, for which the sail is placed perpendicular to the direction of sunlight. Figure 4b shows a side view of the acceleration bubble along the $\hat{\boldsymbol{p}}$-axis. As an example, it includes two solar-sail acceleration vectors: one feasible and one unfeasible acceleration vector. The vector that extends up to the bubble surface is feasible, the one that extend beyond it is unfeasible unless the performance of the sail (a_0) is increased. Indeed, the size of the bubble depends on the reference performance of the sail a_0. Hence, varying a_0 around the reference value modifies the size of the acceleration bubble (*i.e.*, we can change the magnitude of the solar-sail acceleration for a given orientation) further increasing the control authority of the solar sail. However, note that, no matter how much a_0 is increased, the sail cannot generate an acceleration component towards the Sun (i.e., along the negative $\hat{\boldsymbol{S}}$-axis).

Variations in a_0 may be achieved with a heliogyro-type solar sail or a fixed-shape sail equipped with reflectivity control devices (RCDs). The heliogyro sail configuration resembles the rotor of a helicopter: the sail membrane is divided into several long slender blades that are deployed and maintained by spinning the sailcraft. Contrary to the fixed-shape sail, these blades can be independently pitched with respect to the incoming sunlight, which, in theory, grants the heliogyro more control authority [23]. The RCDs are thin devices that are attached to the sail membrane [1] and can change their reflectivity upon electric excitation [24]. The RCDs enable variations in both a_0 and the orientation

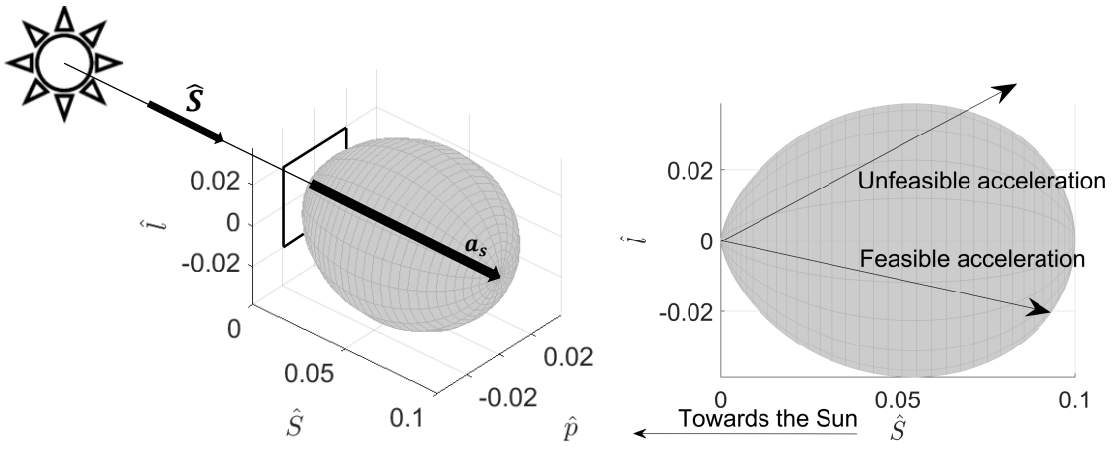

a) **b)**

Fig. 4 Schematics of a) the acceleration bubble of the reference solar sail, and b) side-view indicating feasible and unfeasible $\boldsymbol{a_s}$ vectors.

of the solar-sail acceleration vector [25]. However, both the heliogyro-type sail and the use of RCDs can only enable a downscaling of a_0: the heliogyro configuration can downscale a_0 all the way down to zero, effectively switching the sail off, whereas RCDs can only downscale a_0 to a certain value, which depends on the percentage of the sail surface covered with RCDs.

In this investigation, due to the distance of the EMS from the Sun, we assume that the direction of sunlight remains parallel to the ecliptic even when the sailcraft moves out of the ecliptic. As we will see, the maximum out-of-plane displacement of the DC orbits is approximately four Earth-Moon (EM) distances. If we neglect i_{off}, the angle between the Sun-sail line and the ecliptic when the solar sail is at its maximum out-of-plane distance is approximately 0.6 deg, which yields an error in the solar-sail acceleration of 0.01 %. Thus, it is justified to assume that the $\hat{\boldsymbol{l}}$-axis remains parallel to the ecliptic north pole no matter where the solar sail is within the EMS. Therefore, with the definition of γ and φ as in Fig. 3b, the solar-sail acceleration in frame S can be derived as:

$$\boldsymbol{a_s}\big|_S = a_0 \left(\frac{a_h}{r_4}\right)^2 (\cos\gamma\cos\varphi)^2 \begin{bmatrix} \cos\gamma\cos\varphi \\ \cos\gamma\sin\varphi \\ \sin\gamma \end{bmatrix} . \tag{13}$$

In order to substitute Eq. (13) into Eq. (2), we need to express $\boldsymbol{a_s}$ in frame C. This transformation is obtained by means of the same sequence of rotations introduced in Eq. (10):

$$\boldsymbol{a_s} = \mathrm{R_z}(-\theta)\mathrm{R_y}(-i_{off})\mathrm{R_z}(\theta_h)\,\boldsymbol{a_s}\big|_S . \tag{14}$$

Recall that $\mathrm{R_z}(\theta_h)$ accounts for the motion of the barycenter around the Sun, $\mathrm{R_y}(-i_{off})$ for the offset between the EMS and ecliptic planes, and $\mathrm{R_z}(-\theta)$ for the rotation of C within the orbital plane of the EMS.

C. True Anomalies of the Earth and Moon

To numerically integrate Eq. (1), expressions for θ and θ_h are needed as Eqs. (4), (5), (8), (10) and (11) explicitly depend on θ, θ_h or both. A direct relation between θ_h and the dimensionless time (t) does not exist. However, the heliocentric orbit of the EMS-barycenter is a Keplerian ellipse that obeys the equations of the two-body problem. Therefore, solving Kepler's equation at every integration step provides θ_h as a function of time [20]. To do so, the mean anomaly (M_h) is required, which is computed by retrieving the dimensional time ($t^* = t/n$) and multiplying by the mean motion of the barycenter's heliocentric orbit ($M_h = n_h t^*$).

$$M_h = E_h - e_h \sin E_h \tag{15}$$

$$\theta_h = 2\,tan^{-1}\left[\sqrt{\frac{1+e_h}{1-e_h}}\tan\left(\frac{E_h}{2}\right)\right]. \tag{16}$$

At every integration step, Eq. (15) is numerically solved for the eccentric anomaly (E_h), after which Eq. (16) is employed to obtain θ_h. Since we are not interested in the values of the angles themselves (i.e., we only use them to evaluate trigonometric functions), the proposed methodology does not require any kind of quadrant check or test for ambiguity in the angles.

Given that the orbit of the Moon has been modeled as a Keplerian ellipse as well, a similar procedure can be used to compute θ from t. Notice that the dimensionless time directly represents the mean anomaly of the Moon's orbit (M) since $t = n\,t^*$. However, dealing with two non-linear equations at every integration step is computationally expensive. We therefore consider the expanded state vector, $\widetilde{\boldsymbol{X}} = [\,\boldsymbol{r} \quad \dot{\boldsymbol{r}} \quad \theta\,]^\intercal$. Its expanded derivative ($\tilde{\boldsymbol{f}}$) can be constructed with Eq. (4), inasmuch as it provides the relationship $\dot{\theta}$ as a function of θ. In this way, we trade one non-linear equation for one extra first-order differential equation; numerical integration of the expanded state (with the extra initial condition $\theta(0) = 0$) then provides θ at every integration step.

III. Distant-Circular orbit family

This section derives the novel family of DC solar-sail periodic orbits in the low-fidelity SgC dynamical framework (*i.e.*, the *reference* orbits in Fig. 1a). It also presents a basic coverage analysis of these new orbits for observation of the poles of the Earth and Moon as well as a qualitative discussion concerning the dynamical perturbations that arise in the HF dynamical framework.

A. Periodicity and Symmetry Conditions

First of all, let us review the periodicity and symmetry conditions that must be respected to allow for solar-sail periodic orbits to exist in the EMS. For the sake of clarity, we base the following discussion on the simplest dynamical framework, the solar-sail CR3BP. The apparent motion of the Sun around the barycenter (see Fig. 1b) introduces a time dependency in the EoM, which requires all periodic solar-sail orbits to have a period commensurable with the synodic lunar month ($2\pi/\Omega_4$). Concerning the symmetry, the dynamics of the traditional CR3BP are symmetric with respect to both the (x, z)-plane and the (x, y)-plane [26]. The introduction of the solar-sail acceleration can break the (x, y)-plane symmetry when an out-of-plane component of the solar-sail acceleration is applied, which is the case for the DC orbits. However, the (x, z)-plane symmetry has to be respected, so that the accumulated effect of the solar-sail acceleration after one orbit revolution is zero (*i.e.*, the time-variation of the energy of the orbit must be periodic). Thus, the control law must be symmetric with respect to the initial Sun-sail line (*i.e.*, the $\hat{\boldsymbol{x}}$-axis) as well as periodic with a period commensurable with $2\pi/\Omega_4$ [14]. To this end, the DC orbits employ a simple control law in which the attitude of the solar sail is kept constant with respect to the incoming sunlight, though pitched in the out-of-plane direction (*i.e.*,

$\boldsymbol{u_{DC}} = [\,\gamma \quad 0 \quad 0.1\,]^\intercal$ and $\dot{\boldsymbol{u}}_{\boldsymbol{DC}} = 0$).

Symmetrical periodic solar-sail orbits with a constant control law do not exist for dynamical frameworks more complex than the SgC framework. The SgC framework differs from the solar-sail CR3BP only in the Sun's gravitational perturbation. Since $\boldsymbol{a_4}$ is defined through $\hat{\boldsymbol{S}}$, it is a periodic perturbation and does not break the symmetry conditions. Conversely, in both the SgE and HF frameworks, non-periodic asymmetrical perturbations arise that, if not counteracted, forbid periodic motion. Consider, for example, the addition of the eccentricity of the Moon's orbit (*i.e.*, the SgC→SgE migration). Despite the fact that the motion of the Moon is periodic and symmetric with respect to the (x, z)-plane, its perturbation over an orbit of period $2\pi/\Omega_4$ is not, because the synodic and sidereal months are non-commensurable; when the solar sail completes one orbit, the dynamics do not return to the same initial condition (*i.e.* the Moon is not at perigee). The SgC is therefore taken as the *reference dynamical framework* in which the reference DC orbits are computed.

B. Generation of the Distant-Circular Orbit Family

Following the approach in [14], we start from a classical CR3BP orbit with a suitable period, which in this case is a "circular" orbit confined to the (x, y)-plane with $r \sim 5.6$, period $2\pi/\Omega_4$ and $\gamma = 90$ deg (i.e., the sail is deactivated as it is parallel to the direction of sunlight). We choose the crossing of this orbit with the (x, z)-plane either along the negative ("left") $\hat{\boldsymbol{x}}$-axis or positive ("right") $\hat{\boldsymbol{x}}$-axis as initial condition. Table 2 shows the numerical value of the left and right initial conditions of the classical orbit. The initial position (x, y, z) and velocity $(\dot{x}, \dot{y}, \dot{z})$ components are given as well as the γ angle. Note that both initial conditions are part of the same classical orbit. Then, we use a differential corrector scheme in parallel with a slow continuation of the Sun's parameter μ_4 to migrate the classical orbit to the SgC dynamical framework (i.e., a CR3BP→SgC migration without solar-sail acceleration). The differential corrector iteratively adjusts the initial conditions so that a new periodic orbit is found that holds for an ever-increasing value for μ_4. At the end of the process, the parameter μ_4 is fully introduced and the new orbit holds in the SgC dynamical framework. The precise formulation of the corrector is omitted here for brevity, but can be found in [14]. Figure 5a depicts the continuation process. The outer orbit (dark red orbit) is the classical orbit in the CR3BP framework. As μ_4 is increased, the orbit moves inward to counteract the ever-increasing perturbation from the Sun with an extra gravitational pull from the Earth and Moon.

Table 2 Initial conditions of the classical orbit (CR3BP framework) at the left and right $\hat{x}$-axis crossings.

$\hat{\boldsymbol{x}}$ crossing	x	y	z	$\dot{x}$	$\dot{y}$	$\dot{z}$	γ [deg]
Left	-5.63345502708842	0	0	0	5.21208088110920	0	90
Right	5.63346426702074	0	0	0	-5.21209541560462	0	90

Table 3 gathers the initial conditions of the migrated classical orbit in the SgC framework. Contrary to Table 2, these initial conditions represent two distinct orbits (referred to as left and right seed orbits). Although both orbits lay

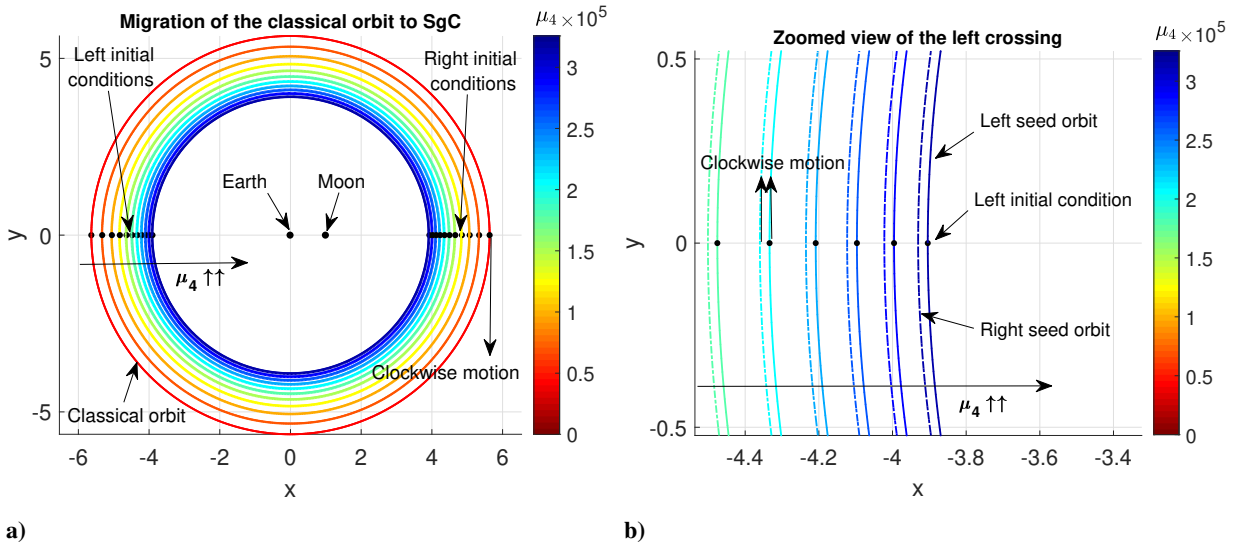

Fig. 5 a) CR3BP→SgC migration of the classical orbit, and b) zoomed view of the left crossing.

very close to one another and are contained in the (x, y)-plane, they are different. Figure 5b provides a zoomed view of the left initial condition to show the difference between the orbits (the continuous and dashed lines represent the left and right seed orbits, respectively). The slight difference between the orbits is caused by the difference in the Sun-spacecraft configuration at the initial time. At $t_0 = 0$, the Sun is located along the negative $\hat{\boldsymbol{x}}$-axis (i.e., to the left of the barycenter, see Fig. 2), whereas the initial conditions are at either side of the barycenter. Hence, the Sun's gravitational pull is slightly stronger on the left initial condition, which ultimately causes the continuation to yield two distinct orbits in the SgC framework, although both orbits originated from the same classical orbit in the CR3BP framework.

Table 3 Initial conditions of the left and right seed orbits (SgC framework).

$\hat{\boldsymbol{x}}$ crossing	x	y	z	$\dot{x}$	$\dot{y}$	$\dot{z}$	γ [deg]
Left	-3.89559177554723	0	0	0	3.60423335920110	0	90
Right	3.92178539480811	0	0	0	-3.62850492952281	0	90

To compute the family of DC orbits, the differential corrector scheme is used again, but with a slow continuation on the attitude angle γ. Variations in the angle γ do not break the required (x, z)-plane symmetry and provide an out-of-plane component of the solar-sail acceleration, which we used to vary the out-of-plane distance of the DC orbits. The starting points for the continuation are the left and right seed orbits (initial conditions in Table 3), which hold in the SgC framework. Recall that the seed orbits exist without a solar-sail acceleration because γ is set to 90 deg (i.e., the sail is placed parallel to the direction of sunlight). The continuation decreases the angle γ by a small amount $\delta\gamma$ and the differential corrector finds a new orbit that holds for the reduced value for γ. By continuing this process until $\gamma = 0$ deg, the right and left DC sub-families, parameterized in γ, arise. Note that, in this second continuation, we do not vary any dynamical parameter; the whole process occurs in the SgC framework.

The sub-families are depicted separately in Figs. 6a and b and together in Fig. 6c. The initial conditions (indicated with black dots in Fig. 6a-c) of the sub-family in Fig. 6a lie along the negative $\hat{\boldsymbol{x}}$-axis (referred to as left DC orbits), while those of the sub-family in Fig. 6b lie along the positive $\hat{\boldsymbol{x}}$-axis (referred to as right DC orbits). Both sub-families originate from the two mentioned seed orbits, depicted in Fig. 6c as the darkest blue orbits although the seed orbits are indistinguishable due to their proximity (see Fig. 5b). Recall that the angle γ is bounded to the interval $[-90, 90]$. At 0 deg, the solar-sail acceleration is maximum but does not have a component out of the (x, y)-plane. As γ increases, the out-of-plane component increases until it reaches a maximum at ±35.26 deg. Subsequently, it decreases until, at ±90 deg, the solar-sail acceleration magnitude is zero. When γ is positive/negative, the out-of-plane component points along the positive/negative $\hat{\boldsymbol{z}}$-axis, which yields orbits above and below the EM orbital plane ((x, y)-plane), respectively. We distinguish these orbits as northern and southern orbits accordingly. The southern orbits exist for $\gamma \in [-90, 0]$, whereas the northern orbits exist for $\gamma \in [0, 90]$. Taking advantage of the symmetry, the angle γ appears as an absolute value in Fig. 6 to represent both the northern and southern orbits at the same time. Note that all DC orbits in both sub-families (left and right, north and south) exist for $a_0 = 0.1$, $\varphi = 0$ and have a period of one synodic month ($2\pi/\Omega_4$).

The DC orbits resemble circular orbits that have been displaced out of the (x, y)-plane by the solar-sail acceleration. Indeed, as the angle γ decreases and thus the solar-sail acceleration increases, both left and right DC orbits move out of the (x, y)-plane. However, the orbits in the left DC sub-family are pushed away from the EMS-barycenter, whereas the orbits in the right DC sub-family are pulled towards it. As explained for the seed orbits, this behavior is caused by the initial Sun-sail configuration. Recall that, at $t_0 = 0$, the Sun is located along the negative $\hat{\boldsymbol{x}}$-axis. Consequently, the solar-sail acceleration vector is contained in the (x, z)-plane with its x component directed along the positive $\hat{\boldsymbol{x}}$-axis. Since the initial conditions of the left and right DC orbits are at either side of the barycenter, the solar-sail acceleration contributes to an inward (towards the barycenter) acceleration for the left DC orbits, while the opposite holds for the right DC orbits. The left/right DC orbits therefore move away/towards the barycenter so that the combined gravitational pull of the Earth and Moon compensates for this imbalance in the total acceleration acting on the sailcraft.

To end this section, Fig. 6d shows the evolution of the linear stability as a function of the angle γ for both DC sub-families and seed orbits. All orbits are linearly unstable because the module of the largest eigenvalue of the monodromy matrix (λ_{max}) is greater than unity for all values for γ [20]. Hence, none of the DC orbits can be maintained for a long period of time without an active control strategy. Finally, note how increasing the solar-sail acceleration (i.e., reducing γ) stabilizes the left DC orbits while it produces the opposite effect for the right DC orbits.

C. Coverage Analysis

The large out-of-plane displacement of the DC orbits suggests their potential for polar observation. To asses their coverage capabilities, the sailcraft elevation and range with respect to the Earth's north pole and lunar south pole are computed for 12 orbital revolutions (*i.e.*, approximately one year). Figure 7 presents the results for four selected orbits,

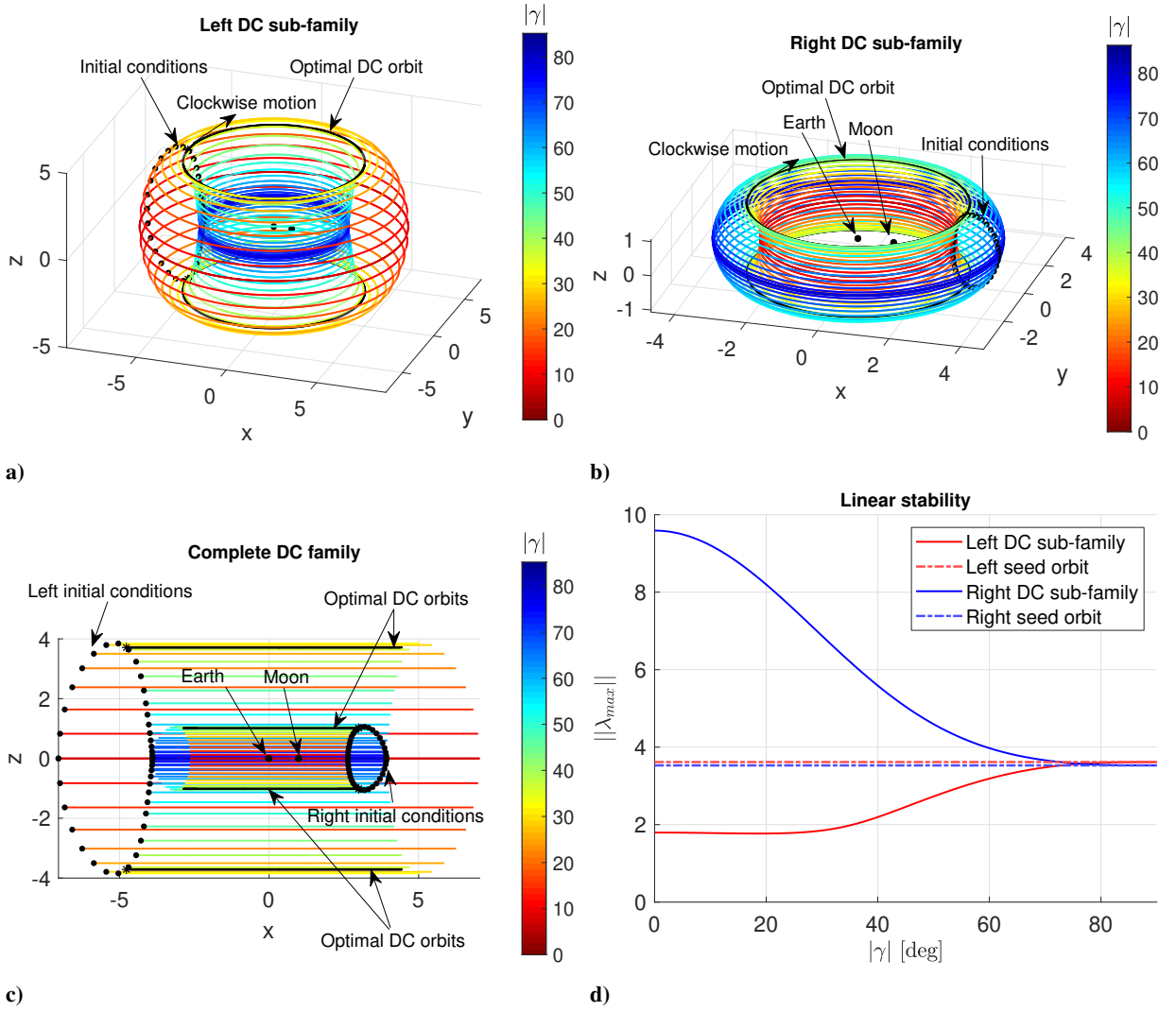

Fig. 6 Family of solar-sail DC orbits and optimal reference orbits (black) for coverage of the poles of the Earth and Moon: a) left DC sub-family, b) right DC sub-family, c) complete family, and d) linear stability.

which are selected based on the fact that they exhibit the largest initial elevation angle. We refer to these orbits as the northern and southern left optimal distant-circular (ODC) orbits and right ODC orbits and they exist for $\gamma_L \simeq \pm 33$ deg and $\gamma_R \simeq \pm 40$ deg, respectively (*i.e.*, the orbits depicted in black in Fig. 6). Table 4 gathers the initial conditions of the northern left and right ODC orbits. In Fig. 7, the results for the reference ODC orbits are represented with dashed black lines; the solid blue lines are discussed later and are not relevant for this section. We employ the northern orbits for coverage of the Earth's north pole, while the southern ones are used for coverage of the lunar south pole. However, it is also possible to use only one orbit for northern (or southern) polar coverage of both bodies. Note that the results can be easily extrapolated to the other poles (*i.e.,* the Earth's south pole and the lunar north pole) due to the symmetry of the problem.

The coverage results for the left ODC orbits are shown in Figs. 7a and c. The left northern ODC orbit provides

Table 4 Initial conditions of the left and right northern ODC orbits (SgC framework).

$\hat{x}$ crossing	x	y	z	$\dot{x}$	$\dot{y}$	$\dot{z}$	γ [deg]
Left	-4.76930535345712	0	3.71099414428400	0	4.41256766476912	0	32.9988292503133
Right	2.99398865438595	0	1.01463755084450	0	-2.77018265007764	0	39.9705182968454

continuous coverage of the Earth's north pole (see Fig. 7a), whereas the left southern ODC orbit achieves the same for the lunar south pole (see Fig. 7c). Both northern and southern left ODC orbits maintain continuous coverage throughout the whole year, reaching a minimum elevation of 14 deg and 25 deg for the Earth's north and lunar south poles, respectively, during the first orbit. The variation of the elevation is explained as follows; as an example, consider Fig. 7a. The elevation increases steadily because the polar axes precess when viewed in the reference frame C at a rotational rate n; the axes thus seem to chase the solar sail along its orbit. The observed drift is then due to the difference between n and the sailcraft's angular rate Ω_4. Concerning the range of the left ODC orbits, it varies between 5.5 and 6.9 Earth-Moon distances with respect to the lunar south pole (see Fig. 7c) and is more constant at approximately six Earth-Moon distances with respect to the Earth's north pole (see Fig. 7a). The larger oscillations in the range with respect to the Moon are due to the larger distance of the Moon with respect to the barycenter.

The coverage results for the right ODC orbits are shown in Figs. 7b and d. Although the right ODC orbits cannot be used for continuous observation of the Earth's north pole (note the negative elevation in Fig. 7b at the start of the sixth orbit revolution), their smaller size grants them better performance (in terms of range and thus spatial resolution) for observing the lunar south pole. The right southern ODC orbit reaches a minimum elevation of 7 deg during the seventh orbit (Fig. 7d), while its range varies between 2.2 and 4.4 Earth-Moon distances.

The main drawback of the ODC orbits is their remoteness from the primaries. In [15], the spatial resolution provided by the clover-shaped and vertical Lyapunov orbits is computed with respect to the Earth's north pole and lunar south pole, respectively. The authors assume a linear relation between range, wavelength (0.5 μm) and imager aperture diameter (0.5 m), which leads to an image resolution of the order of 1.2 km at a range of 1.3 Earth-Moon distances for the clover-shaped orbit and 0.3 km at a range of 0.3 Earth-Moon distances for the vertical Lyapunov orbit. Because of the mentioned linear relation, we can extrapolate these values to the ODC orbits to give an idea of how image resolution deteriorates for these orbits. At an average range of 6 and 3 Earth-Moon distances, the left and right ODC orbits provide an image resolution of the order of 5.5 km and 2.8 km, respectively. We do not distinguish between the Earth's north and lunar south poles because the average range is approximately the same for both cases (see Fig. 7). To increase the image resolution, a larger aperture diameter would be required, the associated mass increment of which may yield an unreasonably large solar sail to maintain the solar-sail acceleration at the required magnitude.

The main advantage of the ODC orbits is their temporal resolution. The left ODC orbits achieve continuous coverage of both the Earth and lunar poles throughout the year, while the right ODC orbits only for the lunar poles.

"Traditional" missions for polar observation of the Earth and Moon rely on constellations of at least two satellites to achieve continuous coverage [27]. By using the ODC orbits, this can be achieved with just one sailcraft (i.e., the ODC orbits sacrifice spatial resolution for temporal resolution in the ever-present trade-off between these metrics).

Rather than for scientific observations or imaging, the ODC orbits could be used for laser communications between a future lunar base located at the lunar south pole and the Earth. The left southern ODC orbit provides continuous coverage of both the Earth's and lunar south poles at the same time. Imagine that, instead of a camera, the solar sail is equipped with stabilized laser reflectors. A laser beam could be sent to the solar sail orbiting above the lunar south pole, which then would be reflected towards the Earth. The beam could be received either by a ground station located near the south pole or a satellite-based system. This way, a continuous link between the lunar base and the Earth could be established with just a single sailcraft. Of course, this is entirely theoretical. To our knowledge, a laser beam has never been reflected mid-way in outer space using reflectors for communication purposes. However, laser communications between the Earth and a spacecraft orbiting the Moon have been tested and proved not only feasible but better than traditional radio links [28]. Furthermore, high quality pocket-size laser retro-reflectors are widely used in the field of laser ranging [29]. It would be required to adapt and migrate this technology to the specific task at hand: a highly stabilized laser reflector of small mass with tight aiming constraints. Compared to the technological readiness level of solar sails, it does not seem impossible that such a system could be developed in parallel in the near future.

D. Perturbing Acceleration

The difference between any two dynamical frameworks depicted in Fig. 1a resides in the accelerations acting on the sailcraft. For discussion purposes, we assume that $\ddot{\boldsymbol{r}}(t)$ is the total acceleration acting on the sailcraft along a certain reference orbit in the SgC framework. If we compute the total acceleration along the same reference orbit but in the HF dynamical framework, we would obtain a different acceleration $\ddot{\boldsymbol{r}}'(t)$. The difference between these two, $\Delta\boldsymbol{a}(t) = \ddot{\boldsymbol{r}}'(t) - \ddot{\boldsymbol{r}}(t)$, is what we call the perturbing acceleration, which is composed of several terms dependent on the dynamical parameters e, e_h and i_{off}. Recall that these parameters are set to zero in the SgC framework, deactivating the perturbations. The key point is that, if we want to follow the exact same reference orbit under the HF dynamics, the solar sail must counteract the perturbing acceleration . To achieve that, the reference constant control law must be modified and become time-dependent. We refer to the solar-sail acceleration that results from the new control law as the solar-sail counter acceleration. It has to be equal to the solar-sail acceleration due to the reference control law plus a term that cancels out the perturbing acceleration: $\boldsymbol{a}_{\boldsymbol{s}}''(t) = \boldsymbol{a}_{\boldsymbol{s}}'(t) - \Delta\boldsymbol{a}(t)$, where $\boldsymbol{a}_{\boldsymbol{s}}''(t)$ is the solar-sail counter acceleration and $\boldsymbol{a}_{\boldsymbol{s}}'(t)$ is the solar-sail acceleration due to the reference control law in the HF framework. Note the prime in $\boldsymbol{a}_{\boldsymbol{s}}'(t)$; this term differs from the solar-sail acceleration in the SgC framework ($\boldsymbol{a}_{\boldsymbol{s}}$) because the plane offset (i_{off}) moves the Sun out of the Earth-Moon plane (i.e., the $\hat{\boldsymbol{S}}$ vector in Eq. (12) differs between both frameworks, see Fig. 2). Recall that the reference control law is defined with respect to the $\hat{\boldsymbol{S}}$ vector, which causes the difference between $\boldsymbol{a}_{\boldsymbol{s}}$ and $\boldsymbol{a}_{\boldsymbol{s}}'$.

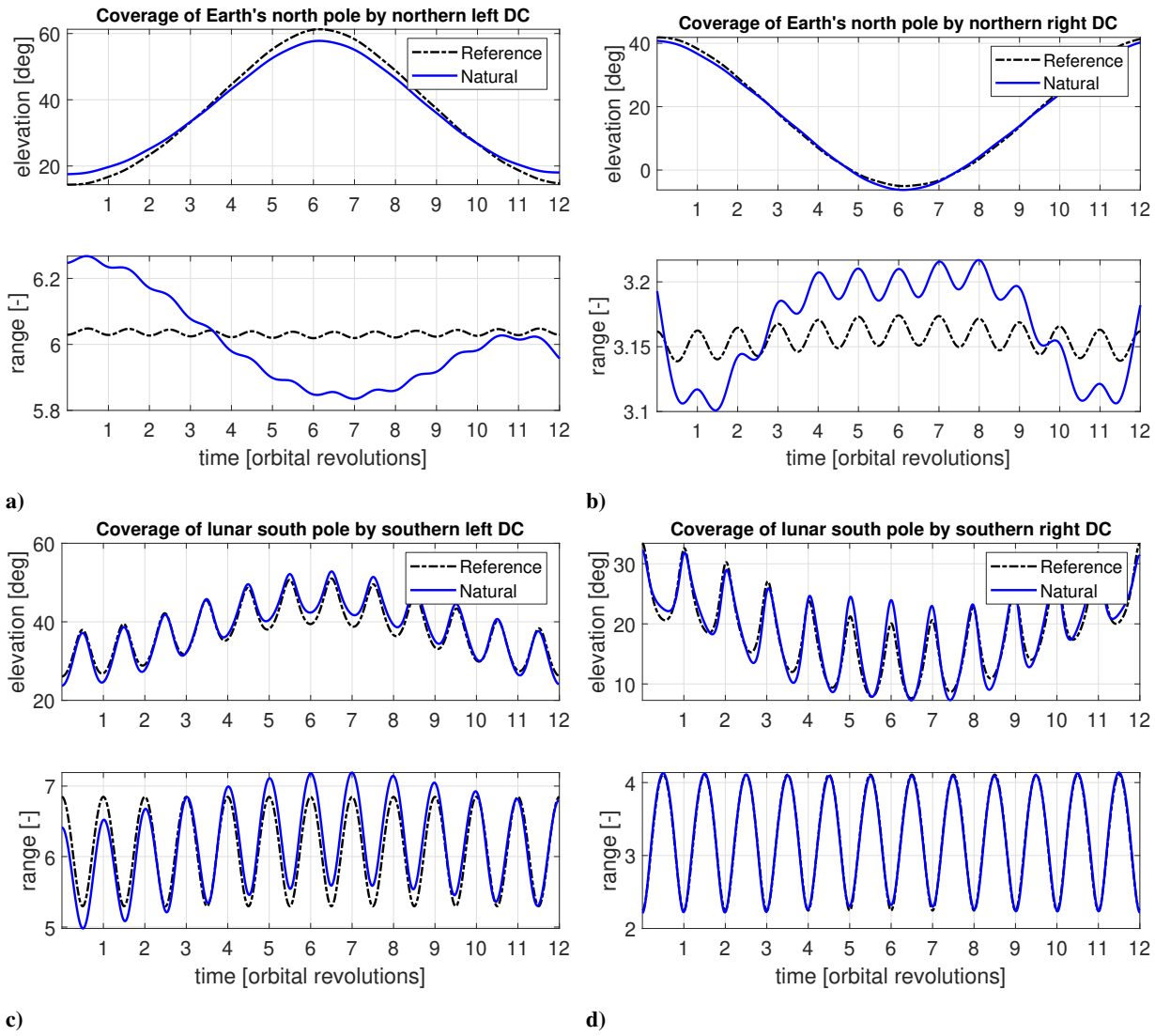

Fig. 7 Elevation and range of the optimal (reference and natural) ODC orbits: a-b) left and right northern ODC orbits with respect to the Earth's north pole, and c-d) left and right southern ODC orbits with respect to the lunar south pole.

Fig. 8 shows the magnitude of the perturbing acceleration (i.e., $||\boldsymbol{\Delta a}(t)||$), in the HF framework) acting on the two right ODC orbits depicted in Fig. 6b over the course of one year; for comparison, the separate contributions by e and $i_{off} + e_h$ are also provided. Note that the perturbing acceleration over the two right ODC orbits only differs in orientation, having the same magnitude in both cases. The eccentricity of the Moon's orbit (e) introduces perturbations (i.e., variations in acceleration) in the gravitational pull of the Earth and Moon as well as in the rotational term, which are combined in the term Δa_e. Similarly, $\Delta a_{ioff,eh}$ gathers the perturbations induced by the plane offset (i_{off}) and the heliocentric eccentricity (e_h), parameters that appear and modify the expressions for the accelerations $\boldsymbol{a_s}$ and $\boldsymbol{a_4}$ in Eq. (2) when activated in the HF framework. From Fig. 8, one can appreciate that the term Δa_e is one order of magnitude larger than $\Delta a_{ioff,eh}$ (note the difference in scale between the left and right vertical axes).

Fig. 8 indicates that, to counteract the perturbations induced by the Moon's eccentricity, the reference value $a_0 = 0.1$ has to be increased, at least, fourfold. However, it might be possible to counteract the perturbing accelerations represented by $\Delta a_{ioff,eh}$, since its magnitude is smaller than that of a_0. Finally, for the left ODC orbits, the quasi-periodic pattern of the perturbing acceleration is identical. However, the average magnitude of Δa_e is larger (*i.e.*, approximately 0.6) and that of $\Delta a_{ioff,eh}$ is smaller (*i.e.*, approximately 0.004) because of the larger radial distance from the barycenter for these orbits.

Additional information concerning the direction of the perturbing acceleration vector is displayed in Fig. 9. This graph combines the solar-sail acceleration bubble with a sample of the required solar-sail counter-acceleration $\boldsymbol{a_s''}$, all displayed in frame S. Figure 9 only shows the results for the northern right ODC orbit as the results for the remaining ODC orbits are similar. Recall that the acceleration bubble represents the envelope of all possible solar-sail acceleration vectors [22]. Although we can enlarge the bubble by augmenting a_0, it is impossible to generate accelerations towards the Sun (*i.e.*, in negative $\hat{\boldsymbol{S}}$ direction). Hence, it is clear from Fig. 9 that the perfect SgC→HF migration, where the solar sail counteracts all perturbations of the HF dynamical framework to perfectly follow the reference orbits is impossible; an additional propulsion system would be required for that purpose.

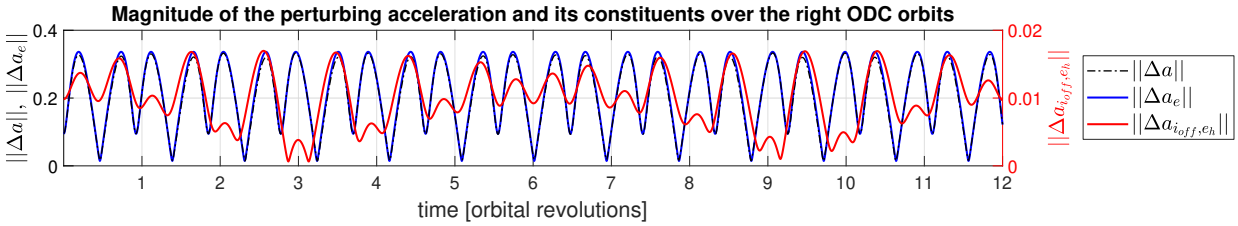

Fig. 8 Magnitude of the perturbing acceleration in the SgC→HF migration and the contributions due to e and $i_{off} + e_h$ for the right ODC orbits.

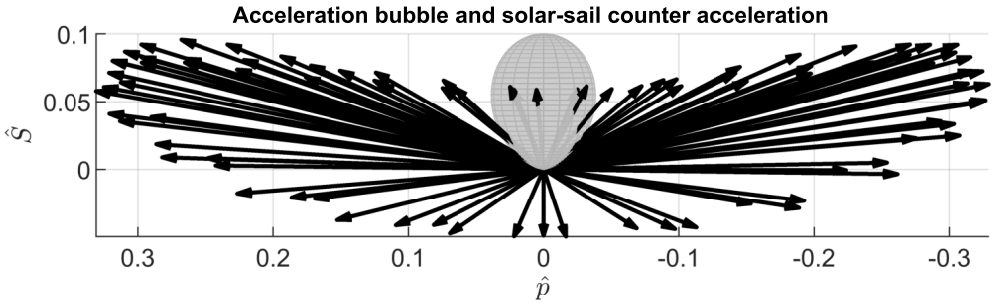

Fig. 9 View from the positive $\hat{I}$-axis of the acceleration bubble (grey) and the required solar-sail counter-acceleration a_s'' (black arrows) in the SgC→HF migration for the right northern ODC orbit.

IV. Natural Orbits

In the previous section, we demonstrated that the reference ODC orbits cannot be perfectly tracked in the HF dynamical framework. The perturbations are too strong and act in directions that cannot be counteracted by the solar sail. Moreover, their non-periodic nature prevents the existence of periodic orbits with a constant control law. However, it is still possible to compute nearby open trajectories that hold under the HF dynamics and follow the same simple reference control law. The one-step multiple-shooter differential corrector (OsMSDC) algorithm in parallel with a slow continuation on e, e_h and i_{off} can be used to this end. We refer to the nearby open trajectories as quasi-periodic orbits as they seem to be bounded to the reference orbits. This quasi-periodicity was investigated by numerically propagating the trajectories for 12 orbital revolutions to demonstrate that they remain bounded for a complete cycle of the perturbations.

A. One-Step Multiple-Shooter Differential Corrector

The general idea of the one-step multiple-shooter differential corrector is as follows. Suppose we divide a reference trajectory into $N-1$ segments that are connected through N nodes. Each node represents the trajectory at a particular epoch; it has a state vector and a time variable associated to it. Subsequently, we increase the parameters e, e_h and i_{off} by a small amount and forward propagate the states at the nodes from the time associated with that node to the time associated with the next node. Since the dynamics have changed, the resulting trajectory is open and composed of $N-1$ arcs that do not arrive at the next node (see Fig. 10a). The OsMSDC iteratively modifies the nodes (*i.e.*, state and time at the node) to build a nearby continuous trajectory that holds under the modified dynamics. By repeating this continuation-correction process, trajectories that resemble the original reference orbit and hold under the HF dynamics are found. The OsMSDC algorithm presented here is a modification of the ones used in [30] and [31] in order for it to be applicable to non-autonomous systems. For the following exposition, it is important to point out that we do not consider active control; that is, the control laws are equal to the reference control laws presented in the previous section (*i.e.*, $\boldsymbol{u_{DC}} = [\,\gamma \quad 0 \quad 0.1\,]^\intercal$).

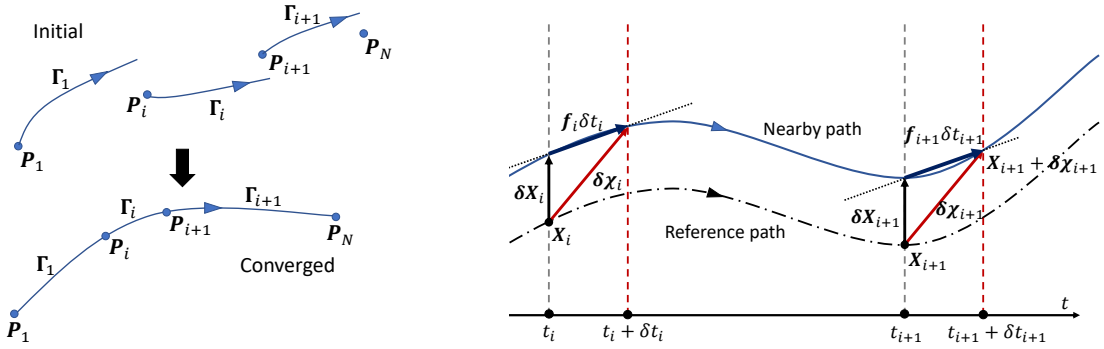

Fig. 10 Schematics of a) the initial and converged trajectories, and b) the contemporaneous and non-contemporaneous trajectory variations (adapted from [27] and [32]).

The targeted continuous trajectory must satisfy the following problem:

$$\boldsymbol{g}_0(\boldsymbol{P}_1) = \boldsymbol{0} \tag{17}$$

$$\boldsymbol{\Gamma}(t_{i+1}|\boldsymbol{P}_i) - \boldsymbol{X}_{i+1} = \boldsymbol{0} \qquad \text{for} \qquad i = \{1, 2, \ldots, N-1\} \tag{18}$$

$$\boldsymbol{g}_f(\boldsymbol{P}_N) = \boldsymbol{0} \tag{19}$$

where Eqs. (17) and (19) represent the constraints imposed on the initial and final nodes and Eq. (18) the continuity constraints. $\boldsymbol{g}_0$ and $\boldsymbol{g}_f$ are generic functions that adopt an explicit expression depending on the particular problem investigated. $\boldsymbol{P}_i = [\, \boldsymbol{X}_i^\intercal \quad t_i \,]^\intercal$ is a node variable and $\boldsymbol{\Gamma}(t_{i+1}|\boldsymbol{P}_i)$ is the last state of a trajectory arc propagated from $\boldsymbol{P}_i$ to time t_{i+1} (see Fig. 10a), *i.e.*:

$$\boldsymbol{\Gamma}(t_{i+1}|\boldsymbol{P}_i) = \boldsymbol{\Gamma}_i = \boldsymbol{X}_i + \int_{t_i}^{t_{i+1}} \boldsymbol{f}(\boldsymbol{X}, t) dt \,. \tag{20}$$

Because, in this section, we consider a constant control law equal to its reference value, we suppress the dependency of $\boldsymbol{f}$ on $\boldsymbol{u}$. If we gather all the nodes in a single vector $\boldsymbol{P} = [\, \boldsymbol{P}_1^\intercal \quad \boldsymbol{P}_2^\intercal \quad \ldots \quad \boldsymbol{P}_N^\intercal \,]^\intercal$, Eqs. (17)-(19) can be written as $\boldsymbol{G}(\boldsymbol{P}) = \boldsymbol{0}$, which, after linearization, becomes:

$$-\boldsymbol{G}(\boldsymbol{P^o}) = \mathrm{J}_{\boldsymbol{G}}(\boldsymbol{P^o})\, \boldsymbol{\delta P} \tag{21}$$

where $\boldsymbol{P^o}$ represents an initial guess for the vector of node variables and $\mathrm{J}_{\boldsymbol{G}}(\boldsymbol{P^o})$ the Jacobian matrix of the constraints evaluated at the initial guess. When solved, this linear system suggests an update for $\boldsymbol{P^*} = \boldsymbol{P^o} + \boldsymbol{\delta P}$ that, after some iterations, should drive $\boldsymbol{G}(\boldsymbol{P^*})$ to zero, thereby, resulting in a continuous trajectory (see Fig. 10a).

The main non-zero elements of the Jacobian are the partials:

$$\frac{\partial(\boldsymbol{\Gamma}_i - \boldsymbol{X}_{i+1})}{\partial \boldsymbol{P}_i} = \begin{bmatrix} \dfrac{\partial \boldsymbol{\Gamma}_i}{\partial \boldsymbol{X}_i} & \dfrac{\partial \boldsymbol{\Gamma}_i}{\partial t_i} \end{bmatrix} \tag{22}$$

$$\frac{\partial(\boldsymbol{\Gamma}_i - \boldsymbol{X}_{i+1})}{\partial \boldsymbol{P}_{i+1}} = \begin{bmatrix} -\mathrm{I}_{6\times 6} & \dfrac{\partial \boldsymbol{\Gamma}_i}{\partial t_{i+1}} \end{bmatrix} \tag{23}$$

which are approximated through the variational equations of $\boldsymbol{\Gamma}_i$. For the remainder of this subsection, which focuses on obtaining the partials on the right-hand sides of Eqs. (22)-(23), we adopt the nomenclature and methods used in [27]. As depicted in Fig. 10b, the total variation in $\boldsymbol{X}_i$ at the nodal epoch t_i is composed of two effects: the change of the state at the epoch t_i and, second, the change of the state due to a variation δt_i in the epoch, namely:

$$\boldsymbol{\delta\chi}_i = \boldsymbol{\delta X}_i + \boldsymbol{f}_i \delta t_i \tag{24}$$

where $\boldsymbol{\delta X}_i$ and $\boldsymbol{\delta\chi}_i$ are the so-called contemporaneous and non-contemporaneous variations of the state $\boldsymbol{X}_i$ at the epoch

t_i. Note that the change due to a variation in the epoch is approximated as the derivative of the state vector times the variation in the epoch (*i.e.*, $\boldsymbol{f}_i \delta t_i$). Furthermore, in accordance with the definition of the state transition matrix (STM) [20], we can relate the contemporaneous variations between two consecutive epochs t_i and t_{i+1} as follows:

$$\boldsymbol{\delta X}_{i+1} = \Phi_i \, \boldsymbol{\delta X}_i \tag{25}$$

where Φ_i is the STM from epoch t_i to epoch t_{i+1} along the path $\boldsymbol{\Gamma}_i$. Then, substitution of Eq. (24) in Eq. (25) yields:

$$\boldsymbol{\delta\chi}_{i+1} - \boldsymbol{f}_{i+1}\delta t_{i+1} = \Phi_i(\boldsymbol{\delta\chi}_i - \boldsymbol{f}_i \delta t_i) \tag{26}$$

which relates all possible variations at epoch t_i with those at epoch t_{i+1}. Moreover, the variation $\boldsymbol{\delta\chi}_{i+1}$ must satisfy the integral relation:

$$\boldsymbol{X}_{i+1} + \boldsymbol{\delta\chi}_{i+1} = \boldsymbol{\Gamma}(t_{i+1} + \delta t_{i+1} | \boldsymbol{X}_i + \boldsymbol{\delta\chi}_i, t_i + \delta t_i) \, . \tag{27}$$

If we assume that the variations are small, we can linearize Eq. (27) and rearrange to obtain:

$$\boldsymbol{\delta\chi}_{i+1} - \frac{\partial \boldsymbol{\Gamma}_i}{\partial t_{i+1}} \delta t_{i+1} = \frac{\partial \boldsymbol{\Gamma}_i}{\partial \boldsymbol{X}_i} \boldsymbol{\delta\chi}_i + \frac{\partial \boldsymbol{\Gamma}_i}{\partial t_i} \delta t_i \, . \tag{28}$$

Finally, by comparing Eq. (28) with Eq. (26), we obtain the desired link between the partials on the right-hand side of Eqs. (22)-(23) with Φ_i, $\boldsymbol{f}_i$ and $\boldsymbol{f}_{i+1}$, which allows us to expand the Jacobian as:

$$\mathrm{J}_{\boldsymbol{G}} = \begin{bmatrix} \mathrm{J}_{\mathrm{g}_0} & 0 & \cdots & 0 \\ \begin{bmatrix} \Phi_1 & -\Phi_1 \boldsymbol{f}_1 \end{bmatrix} & \mathrm{H}_2 & \cdots & 0 \\ 0 & \begin{bmatrix} \Phi_2 & -\Phi_2 \boldsymbol{f}_2 \end{bmatrix} & \cdots & 0 \\ \vdots & \ddots & \ddots & \vdots \\ 0 & \cdots & \mathrm{H}_{N-1} & 0 \\ 0 & \cdots & \begin{bmatrix} \Phi_{N-1} & -\Phi_{N-1} \boldsymbol{f}_{N-1} \end{bmatrix} & \mathrm{H}_{\mathrm{N}} \\ 0 & \cdots & 0 & \mathrm{J}_{\mathrm{g_f}} \end{bmatrix} \tag{29}$$

where $\mathrm{J}_{\mathrm{g}_0}$ and $\mathrm{J}_{\mathrm{g_f}}$ are the Jacobians of the initial and final constraints, respectively, and $\mathrm{H_k} = [-\mathrm{I}_{6\times 6} \quad \boldsymbol{f}_k]$. In the versions of this multiple-shooter differential corrector that work with *autonomous* dynamical systems (see [30] and [31]), the Jacobian matrix is formulated differently because the integration time between two nodes ($\Delta t = t_{i+1} - t_i$) is used as nodal epoch instead of assigning an epoch to each node. Assigning Δt to each node is allowed for autonomous

systems because the same result is obtained when integrating the dynamics from zero to Δt as from t_i to t_{i+1}. However, this is not true for a non-autonomous system, since the initial integration time of each integrated trajectory segment has to correspond to a certain epoch. For example, in our case, starting each trajectory segment propagation from $t = 0$ places the $\hat{\boldsymbol{S}}$ vector aligned with the $\hat{\boldsymbol{x}}$-axis for all nodes, which would be incorrect.

B. Results

It is important to reiterate that all results in this section maintain the constant control law of the reference ODC orbits (*i.e.*, they do not apply active control). To illustrate the effect of the different perturbations on the reference ODC orbits, we analyze two migrations: Fig. 11a corresponds to the SgC→SgE migration, whereas Fig. 11b is the result of the SgC→HF migration. Therefore, the deviations (solid dark blue lines) from the reference ODC orbits (dashed cyan lines) in subplot a) are only caused by the eccentricity of the Moon's orbit (e), while the deviations appearing in subplot b) are the result of all perturbations acting together. We call the resulting open trajectories *e-corrected* and *natural* ODC "orbits", respectively (see Fig. 1a), despite the fact that these "orbits" are, at most, quasi-periodic orbits. The migrations are performed for approximately one year (12 orbital revolutions) so that a complete cycle of the perturbations is taken into account (i.e., after twelve orbital revolutions, the relative positions of the Sun, Earth and Moon are approximately the same). Also, recall that the Earth and Moon wobble around their mean positions along the $\hat{\boldsymbol{x}}$-axis throughout the year, which causes the elongated black Moon in Fig. 11. In all cases, the imposed constraints on the initial and final nodes are:

$$\boldsymbol{g}_0(\boldsymbol{P}_1) \equiv [y_1 \quad t_1]^\intercal = \boldsymbol{0} \tag{30}$$

$$\boldsymbol{g}_f(\boldsymbol{P}_N) \equiv y_N = 0 \tag{31}$$

which force the initial and final nodes to coincide with the (x, z)-plane. In addition, the initial epoch is kept fixed to zero in order for all results to depart from the same initial condition. Conversely, the final epoch is free so that the correction process can adjust this variable to meet the constraints.

Concerning the e-corrected ODC orbits in Fig. 11a, we can appreciate that they barely deviate from the reference orbits: the solid dark blue trajectory and the dashed cyan orbit nearly overlap. Interestingly, these e-corrected orbits appear to demonstrate quasi-periodic behavior as the boundary nodes (*i.e.*, initial and final nodes) of the e-corrected orbits (depicted in Fig. 11a as light green triangles) match almost perfectly. In addition, they also match the boundary nodes of the reference orbits (depicted in red circles) so well that the red circles are not visible in Fig. 11a. Conversely, for the natural ODC orbits in Fig. 11b, a clear discrepancy between the boundary nodes is observable. Moreover, the boundary nodes of the natural orbits no longer match those of the reference orbits. This is interesting as the $i_{off} + e_h$ perturbation is one order of magnitude smaller than the perturbation due to the eccentricity of the Moon. It therefore

seems that the coupling between the perturbations due to $i_{off} + e_h$ and the perturbations due to the eccentricity of the Moon impairs the apparent quasi-periodic motion of the natural orbits. Furthermore, it suggests that elimination of the $i_{off} + e_h$ related perturbations via an active control strategy may allow permanently bounded quasi-periodic orbits, which will be investigated in the next section.

Lastly, to demonstrate the effect of the perturbations on the observation capabilities of the reference ODC orbits, Fig. 7 shows the coverage and range of the natural ODC orbits (solid dark blue lines) in addition to the coverage and range for the reference ODC orbits. We can conclude that, within the considered time-frame, the general coverage capabilities of these orbits are preserved despite the effect of the perturbations.

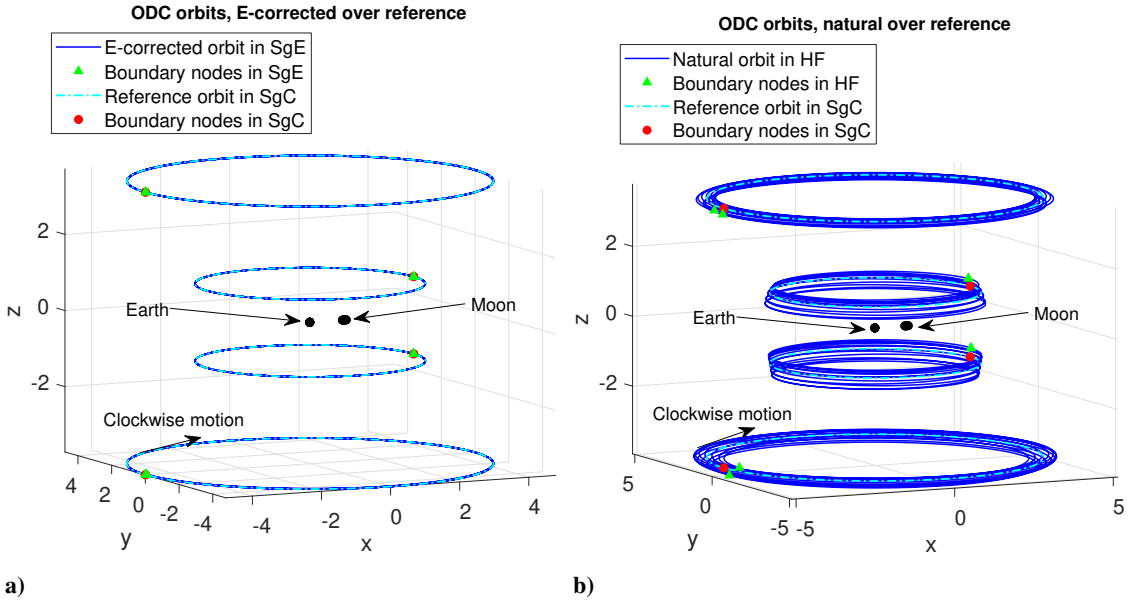

Fig. 11 a) E-corrected ODC orbits (SgC→SgE migration), and b) natural ODC orbits (SgC→HF migration).

V. Controlled Orbits

This section analyzes the controllability of the ODC orbits by computing non-constant, continuous control laws to partially counteract the perturbations (see the *controlled* orbits in Fig. 1a). We have seen that total cancellation of the perturbing acceleration $\boldsymbol{\Delta a}$ is not possible for the SgC→HF migration. Therefore, we seek a compromise between the reference ODC orbits and the natural ODC orbits.

We obtain time-varying control laws in two different ways. First we derive an extended version of the OsMSDC to numerically obtain $\boldsymbol{u}(t)$ during the SgC→HF migration (*i.e.*, the *numerical* control in Fig. 1a). Subsequently, it is shown that the control law to counter the perturbing acceleration introduced in the SgE→HF migration can be obtained analytically, which leads to the second method of computing the controls (*i.e.*, the *analytic* control in Fig. 1a).

A. Weights Optimization

Several minor modifications to the OsMSDC of the previous section are required to permit variations in the reference control law. In the first place, the nodal variables are expanded as $\widetilde{\boldsymbol{P}}_i = [\,\widetilde{\boldsymbol{X}}_i^\intercal \quad t_i\,]^\intercal$, where $\widetilde{\boldsymbol{X}}_i = [\,\boldsymbol{X}_i^\intercal \quad \boldsymbol{u}_i^\intercal\,]^\intercal$ is the expanded state vector and $\boldsymbol{u}_i$ is the control law evaluated at t_i. This causes the partials in Eqs. (22) and (23) to change as:

$$\frac{\partial(\boldsymbol{\Gamma}_i - \boldsymbol{X}_{i+1})}{\partial \widetilde{\boldsymbol{P}}_i} = \begin{bmatrix} \widetilde{\Phi}_i & -\Phi_i \boldsymbol{f}_i \end{bmatrix} \tag{32}$$

$$\frac{\partial(\boldsymbol{\Gamma}_i - \boldsymbol{X}_{i+1})}{\partial \widetilde{\boldsymbol{P}}_{i+1}} = [-\mathrm{I}_{6\times6} \quad 0_{6\times3} \quad \boldsymbol{f}_{i+1}] \tag{33}$$

where $\widetilde{\Phi}_i = [\Phi_i \quad \frac{\partial \boldsymbol{\Gamma}_i}{\partial \boldsymbol{u}_i}]$ is the expanded STM, which can be calculated by substituting the state vector $\boldsymbol{X}_i$ by the expanded state vector $\widetilde{\boldsymbol{X}}_i$ and reformulating the differential equations of the STM accordingly [33].

A second modification is the application of a piece-wise cubic spline interpolation for the controls, which generates a continuous control law in between two nodal epochs after every iteration of the OsMSDC. For example, at initialization, the algorithm is provided with the reference trajectory and its associated constant control law. The latter are sampled at every t_i to obtain the discrete $\boldsymbol{u}_i$. Then, after the first iteration, the nodal controls are updated independently from one another, which results in a discontinuous control law. It is at this point that the interpolation takes place, such that a continuous control law is passed to the next iteration. When convergence is reached, both trajectory and control law are continuous (see Fig. 10a).

The expansion of the nodes with the controls increases the number of variables in Eq. (21). To obtain the natural orbits in the previous section and Fig. 11, the underdetermined linear system in Eq. (21) was solved by choosing the least norm solution (*i.e.*, variations in positions, velocities and epochs participate equally in closing the trajectory). However, in this section we introduce a matrix W that assigns different weights to each component of $\boldsymbol{u}_i$ such that the controls are varied more (or less if $W_i < 1$) intensively than the nodal positions, velocities and epochs, which ultimately yields a less deviated trajectory. Mathematically, the weighting matrix is introduced as:

$$\boldsymbol{\delta P} = \mathrm{W}\,\mathrm{J_G}^\intercal\,(\mathrm{J_G}\,\mathrm{W}\,\mathrm{J_G}^\intercal)^{-1}(-\boldsymbol{G}) \tag{34}$$

where W is a diagonal matrix with the position, velocity and epoch terms equal to one and the control terms equal to W_γ, W_φ and W_{a_0}, where the subscript refers to the control parameter. Although large weights increase the control effort and thus should keep the perturbed trajectory closer to the reference orbit, they also introduce numerical instabilities that impair the convergence of the algorithm. A trade-off needs to be made between numerical and control performances: when the weights are too large, the algorithm diverges; the controls barely counteract the perturbations when the weights are too small. Indeed, smaller weights just reduce the usage of the controls to the limit $W_\gamma = W_\varphi = W_{a_0} = 0$, where the controls are ignored by the algorithm leading to the natural orbits of the previous section and the constant

reference controls. This opens up a variety of options, like leaving one control unchanged or pushing the weights to the convergence limit. In fact, one of the reasons to define the weights as they are (i.e., smaller weights yield less control effort) was to allow the algorithm to easily switch off one control variable if needed. If the inverse definition of the weights would have been adopted (i.e., larger weights yield less control effort), the algorithm would have to drive one weight to infinity to deactivate one control variable. Such behavior is not numerically desirable.

We use the particle swarm optimization algorithm implemented in MATLAB® to select the best values for the weights. The upper bounds of the search space are found by trial and error: with a reasonable value for $\dot{\gamma}$ and $\dot{\varphi}$ of approximately 24 deg/day [34], we force the algorithm manually until the derivatives of the attitude controls just surpass this limit, which then defines the upper bounds. For this particular problem, the obtained upper bounds for the weights were not large enough to cause numerical instabilities and thus convergence issues, which eased the optimization process. The objective function of the optimization algorithm $\mathcal{F}_E$, targets the minimum error solution ($minE$), understanding for error, the normal distance from the reference orbit to the perturbed trajectory (see Fig. 12a). More precisely, $\mathcal{F}_E$ equals the root mean square (RMS) of the normal error along the entire trajectory E_{RMS} (*i.e.*, $\mathcal{F}_E = E_{RMS}$).

The posed optimal control problem is similar in many aspects to the direct collocation and nonlinear programming (DCNLP) approach [35]. As in DCNLP, the trajectory and controls are discretized in N nodes, yielding $N-1$ trajectory segments. Then, the nodes are grouped in the vector $\boldsymbol{P}$, which is used as the independent variable of the constraints. However, the OsMSDC solves the dynamics (represented by Eq. (27)) numerically with an explicit integrator, while in DCNLP, Eq. (27) is solved implicitly with, for instance, Gauss-Lobatto quadrature. The OsMSDC is a shooting algorithm that employs the information in the STM to compute updates of the initial vector $\boldsymbol{P}$, aimed at closing the trajectory. In DCNLP, no shooting is required as the entire trajectory is linked via suitable interpolation functions. The choice of such functions must be done carefully, for they have to appropriately capture the dynamics of the problem. In this work, the OsMSDC algorithm was selected to solve the posed optimal control problem for practical reasons, as it had already been implemented to obtain the natural trajectories, and to investigate the applicability and performance of the weighting matrix introduced in Eq. (34). Future work may focus on using different methods such as DCNLP to shed more light on the problem of the controllability of solar-sail orbits in the EMS.

Some final considerations regarding the OsMSDC algorithm are as follows. In theory, the more nodes along the trajectory, the faster the convergence, because the trade-off between continuity in the trajectory and controls is handled better. Nonetheless, the more nodes, the larger the matrix that has to be inverted to solve Eq. (34). For our case study, a good intermediate situation was found to be 51 nodes per orbit revolution. For the optimizations to run in a reasonable time, three orbit revolutions instead of 12 were used. It turned out that with three orbit revolutions, the overall behavior of the one-year analysis is well represented. Further improvements in performance were obtained by relaxing the OsMSDC convergence criteria at intermediate steps during the continuation on e, i_{off} and e_h. Only in the last step, when e, i_{off} and e_h have reached their final value, the sum over all components of the constraint vector (*i.e.*, $sum(\boldsymbol{G})$) is

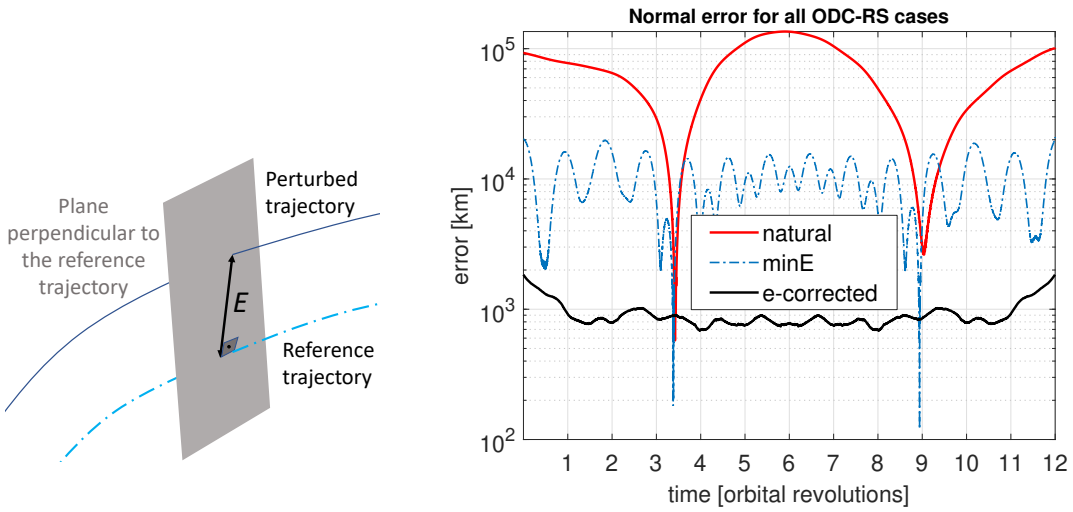

Fig. 12 a) Definition of the normal error E, and b) normal error for all ODC-RS cases.

forced to be less than 1×10^{-8}; in terms of position, this represents a cumulative error of just four meters. This way, the intermediate steps take two-to-three OsMSDC iterations to converge and the last one never surpasses ten. One last remark concerning the algorithm is that the first and last revolutions seem to absorb most of the effect of the perturbations and deviate significantly more than the rest of the trajectory. To palliate this effect, additional pieces of trajectory (i.e., about half an orbit) are added before and after the initial and final nodes, respectively, which are removed after the OsMSDC converges in the last step of the continuation. With the aforementioned settings, one function evaluation took approximately three minutes in a computer equipped with 16 GB of memory and an Intel® Core™ i7-8750H processor.

Note that, for brevity, we do not present the results for all ODC orbits, but only for the southern orbit of the right ODC sub-family (in short, ODC-RS). Fig. 12b shows the normal error curves for all cases in logarithmic scale. The short-period oscillations are related to the rotation of the EMS, whereas the spikes around the third and ninth revolutions correlate to the minima in the component of the perturbing acceleration due to $i_{off} + e_h$ (see Fig. 8, $||\Delta a_{i_{off},e_h}||$ component). Table 5 gathers the normal error statistics for the ODC-RS orbit, which are: the RMS of the normal error (E_{RMS}), minimum error (E_{min}), average error (E_{avg}), and maximum error (E_{max}). In addition to the results for the controlled orbit, the values for the natural ODC-RS orbit and the e-corrected ODC-RS orbit of the previous section are also presented. The table is thus the statistical summary of Fig. 12b.

Table 5 Normal error statistics for all ODC-RS cases.

Orbit type	Perturbations	E_{RMS} (km)	E_{min} (km)	E_{avg} (km)	E_{max} (km)
Natural	None	77030	576	67429	135367
minE	All	10898	120	9957	20885
e-corrected	Only e	974	35	886	2150

Controlling the orbits reduces the maximum error (E_{max}) compared to the natural ODC-RS orbit without significantly modifying the minimum error (E_{min}), indicating that nodes that suffered large deviations in the natural orbit are more readily helped by the controls. Zero error is never reached, which is a consequence of the formulation of the algorithm (i.e., no matter how large the control weights are, all nodes suffer a non-zero deviation at every iteration). Note that the e-corrected ODC-RS orbit has such small errors that even when active control is applied, the algorithm cannot achieve a similar performance when correcting for all perturbing effects. This behavior is better understood with the aid of Fig. 9b. As already commented, this plot displays both the solar-sail acceleration bubble and the required solar-sail acceleration for the SgC→HF migration. Notice that the majority of the solar-sail acceleration vectors require a large component along the $\hat{\boldsymbol{p}}$-axis. Creating an acceleration mainly along the $\hat{\boldsymbol{p}}$-axis requires the sail to be oriented near-parallel to the direction of sunlight, under which condition little thrust is generated. The control algorithm tries to find an intermediate solution in which these perturbations are reduced to the minimum within the thrusting capabilities of the solar sail. Nevertheless, the algorithm does improve the trajectory with respect to the natural orbit. This is partly due to the fact that the accelerations required to counter the effects due to i_{off} and e_h are mostly aligned with the $\hat{\boldsymbol{S}}$-axis and can be effectively countered by the solar sail. This is further explained in the following subsection.

Figure 13 presents the full-year propagation of the *minE* case and its associated control law. Note how the control profiles for the attitude angles (*i.e.*, $\gamma(t)$ and $\varphi(t)$) satisfy the constraint on their rates of change of ±24 deg/day (dashed red lines), which suggests that solar sails can handle the slow-varying perturbations considered in this work. These perturbations are of the order of magnitude of a_0 and vary in accordance with the orbits' time-scale (*i.e.*, one synodic month). We therefore cannot conclude anything about other, faster or potentially stronger, disturbances. However, as proof of the versatility and robustness of the methodology presented in this work, reference [36] successfully applied the control algorithm to other solar-sail periodic orbits in the EMS, in particular to the clover-shaped and vertical-Lyapunov orbits presented in [15].

B. Analytic Control

We have seen that the e-corrected ODC orbits of Fig. 11a perform best in terms of deviation from the reference orbits (see Table 5). However, the e-corrected ODC orbits only account for the e-induced perturbation and not for the perturbations related to $i_{off} + e_h$. Therefore, this section investigates whether we can track the e-corrected ODC-RS orbit in the HF framework so that we only have to counter the perturbations related to $i_{off} + e_h$. We refer to this new problem as the SgE→HF migration, in which the reference ODC-RS orbit in the SgC framework is substituted by the e-corrected ODC-RS orbit in the SgE framework. Fig. 14a depicts the solar-sail acceleration bubble as viewed along the negative $\hat{\boldsymbol{p}}$-axis and a sample of the required solar-sail acceleration to counter the perturbations (black arrows) in this SgE→HF migration. It is clear that with a slight increase of the solar-sail performance, all acceleration vectors can be engulfed by the bubble. The control law required to counter these perturbations can subsequently be computed

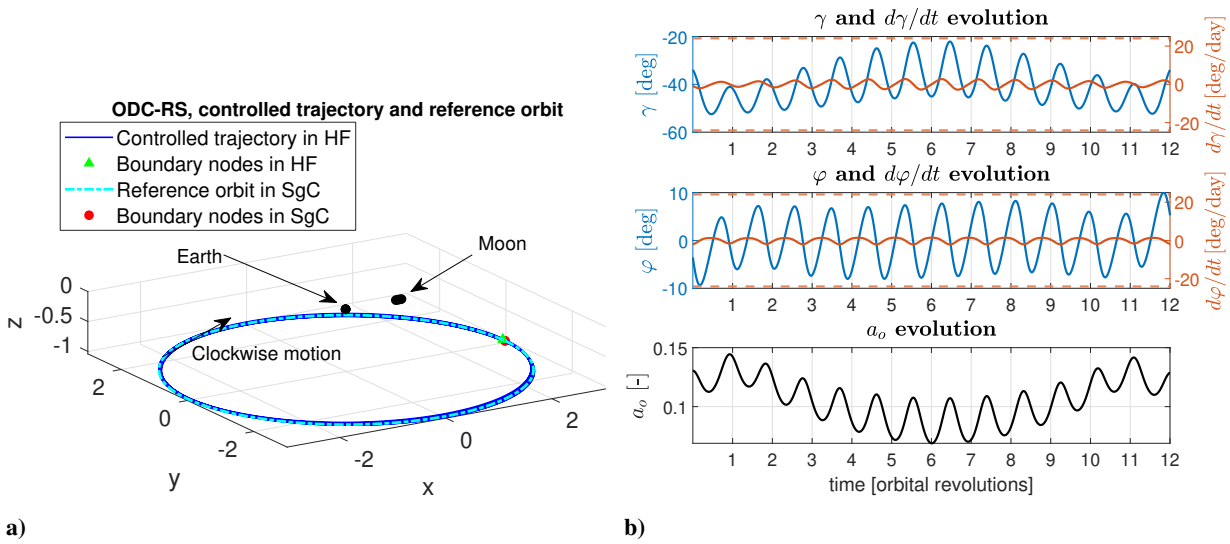

Fig. 13 Trajectory and control law for the *minE* ODC-RS orbit for twelve orbital revolutions.

analytically, the results of which appear in Fig. 14b.

The controls in Fig. 14b again satisfy the maximum angular rates of 24 deg/day and, considering the maximum value for a_0 of 0.14, require an increase in the reference sail's performance of 40 %. With these controls, it is possible to perfectly track the *e*-corrected orbit in the HF framework such that the small errors for the *e*-corrected DC-RS orbit in Table 5 apply in the HF framework. It is thus clear that, for the DC-RS orbit, the strategy of first correcting for the eccentricity without active control and then fully counteracting the remaining perturbations with the analytic control law of Fig. 14b provides the best control solution. However, this is not always the case. As mentioned before, [36] applies the methodology followed in this work to other orbits, showing that, for those orbits where the *e*-related perturbation causes large deviations from the reference orbits, the controls obtained with the OsMSDC yield smaller errors than the analytic control. Therefore, neither approach (*i.e.*, control law computed with theOsMSDC or analytically) outperforms the other in every situation, where the choice has to be made considering the relative magnitude of the different perturbations and their effect on the analyzed reference orbits.

VI. Transfers Between Distant-Circular Orbits

Due to the out-of-plane symmetry in the Earth-Moon system and the availability of a solar-sail induced acceleration, an opportunity exists to transfer between orbits above and below the Earth-Moon orbital plane during a single mission. Such an orbital transfer may significantly increase the mission scientific return. In this section, such transfers are investigated using the weighted OsMSDC algorithm, thereby also demonstrating the versatility of the methodology adopted in this work. Figure 6 suggests that transfers from the northern DC orbits to their southern counterparts could be possible by reducing the angle γ . For instance, consider the northern ODC orbit depicted in black in Fig. 6a with a

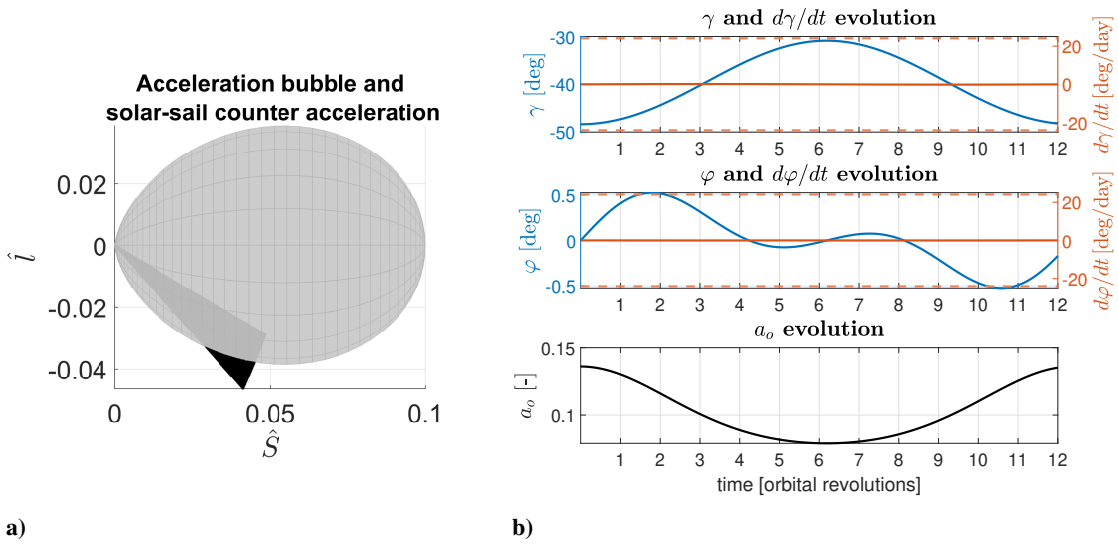

a) **b)**

Fig. 14 SgE→HF migration: a) view along the negative $\hat{p}$-axis of the acceleration bubble (grey) and required solar-sail acceleration (black arrows), and b) ODC-RS analytical control law.

reference value for γ of 33 deg. If γ is reduced, the orbits of the family tend to move towards the (x, y)-plane, following the outer face of the toroid-shaped family (see the red orbits in Fig. 6a). Once in the (x, y)-plane, further reduction of γ (i.e., γ becomes negative) yields increasingly displaced southern orbits until the southern ODC orbit with an angle γ of -33 deg is reached. This behaviour hints at possible transfer trajectories between northern and southern optimal orbits and vice versa. To compute such transfers, we must employ the SgC dynamical framework, since it is the most high-fidelity framework to respect the symmetry with respect to the (x, y)-plane. This property furthermore allows for a convenient simplification, namely that only one half of the transfer needs to be computed (i.e., the final node $\boldsymbol{P}_N$ is located halfway of the complete transfer rather than at the end). The boundary constraints in Eqs. (17) and (19) are therefore modified as follows:

$$\boldsymbol{g}_0(\boldsymbol{P}_1) \equiv \begin{bmatrix} \boldsymbol{X}_1^\intercal & \boldsymbol{u}_1^\intercal & t_1 \end{bmatrix}^\intercal = \begin{bmatrix} \boldsymbol{X}_0^\intercal & \boldsymbol{u}_0^\intercal & t_0 \end{bmatrix}^\intercal \tag{35}$$

$$\boldsymbol{g}_f(\boldsymbol{P}_N) \equiv \begin{bmatrix} y_N & z_N & \dot{x}_N & \boldsymbol{u}_N^\intercal & t_N \end{bmatrix}^\intercal = \begin{bmatrix} 0 & 0 & 0 & \boldsymbol{u}_{\tau/2}^\intercal & \tau/2 \end{bmatrix}^\intercal \tag{36}$$

where τ is the total transfer time, $\boldsymbol{u}_{\tau/2}$ are the controls at $\tau/2$, and the subindexes 1 and N denote the initial and final nodes of the trajectory, respectively. The initial conditions in Eq. (35) must match those of the northern ODC orbits (*i.e.*, the initial state $\boldsymbol{X}_0$, the control law $\boldsymbol{u}_0 = [\,\gamma_0 \quad 0 \quad a_0\,]^\intercal$ and the initial time $t_0 = 0$), while the final conditions in Eq. (36) force the trajectory to cross the $\hat{\boldsymbol{x}}$-axis perpendicularly; by leaving x_N, $\dot{y}_N$ and $\dot{z}_N$ free, the algorithm is allowed to iteratively adjust the value for x at the crossing until it reaches convergence. Finally, considering that the reference control law of the southern orbit is $\boldsymbol{u}_f = [\,-\gamma_0 \quad 0 \quad a_0\,]^\intercal$ and that the control law along the trajectory must be symmetric as well, $\boldsymbol{u}_{\tau/2} = [\,0 \quad 0 \quad a_0\,]^\intercal$.

For the initial guess of the transfer that initializes the OsMSDC algorithm, we assume a linearly varying control law between $\boldsymbol{u}_0$ and $\boldsymbol{u}_f$ over a time-space of τ, which is constrained to be a multiple of the synodic month ($2\pi/\Omega_4$). This is to ensure a correct Sun-sail configuration upon arrival at the southern orbit. Because propagation of $\boldsymbol{X}_0$ with the latter control law does not yield a feasible guess, we introduce $\dot{z}_0 < 0$, where the exact value for $\dot{z}_0$ is determined through trial and error until the propagation crosses the $\hat{\boldsymbol{x}}$-axis after a time $\tau/2$. Furthermore, we first compute a transfer between two almost co-planar DC orbits (*i.e.*, the blue orbits in Fig. 6 with large values for γ) and then apply a continuation in γ to construct transfers between DC orbits displaced ever-further out of the (x, y)-plane. This process leads to the transfers in Fig. 15, in which subplots a) (dahsed cyan line) and b) depict details of a transfer with $\tau = 4(2\pi/\Omega_4)$ between the left ODC orbits of Fig. 6a, whereas subplots c) (dahsed cyan line) and d) provide details of a transfer with $\tau = 3(2\pi/\Omega_4)$ between the right ODC orbits of Fig. 6b. Note that the transfer is initiated after four orbital revolutions and that no variations in a_0 are required.

The smaller out-of-plane distance of the right ODC orbits allows for the faster transfer. However, the required control law is less smooth, since the rapid change in sail attitude at the start of the transfer causes an overshoot. A further reduction of τ requires even more sudden attitude changes, ultimately leading to a surpassing of the imposed maximum rate of 24 deg/day. The transfers shown here are the fastest transfers possible without surpassing this limit. The control laws present a double-symmetry; the accelerations induced during the first half of the transfers have to be exactly reverted during the second half to inject in the southern orbits (recall that the northern and southern orbits employ the same value for γ but with opposite sign). It is important to point out that both transfers can be executed without varying the characteristic acceleration (see the constant value for a_0 in Fig. 15b and d); a simple fixed-shape sail can thus perform the transfer without RCDs or the need to change to the more complex heliogyro architecture.

Finally, note that Figs. 15a and c actually depict two almost superimposed trajectories. As mentioned, the dashed cyan lines are the reference transfers computed in the SgC framework. When migrating these transfers to the HF framework, the trajectories in dark blue are obtained. Indeed, the transfers are also valid in the HF framework; no significant deviations with respect to the reference transfers can be discerned. Note that, when performing the migration to the HF framework, the original initial conditions (red circles in Fig. 15) that hold in the SgC framework are allowed to vary to facilitate the convergence of the OsMSDC.

VII. Conclusions

In this paper, a new family of solar-sail periodic orbits, termed distant-circular (DC) orbits, has been developed for the particular application of polar observation of the Earth and Moon. The orbits exist under the dynamics of the solar-sail circular restricted three-body problem (CR3BP) augmented with the Sun's gravitational perturbation (referred to as the reference dynamical framework). Depending on the initial Sun-sail configuration, the family is further divided into the "left" and "right" sub-families. Moreover, each sub-family is composed of northern and southern orbits (*i.e.*,

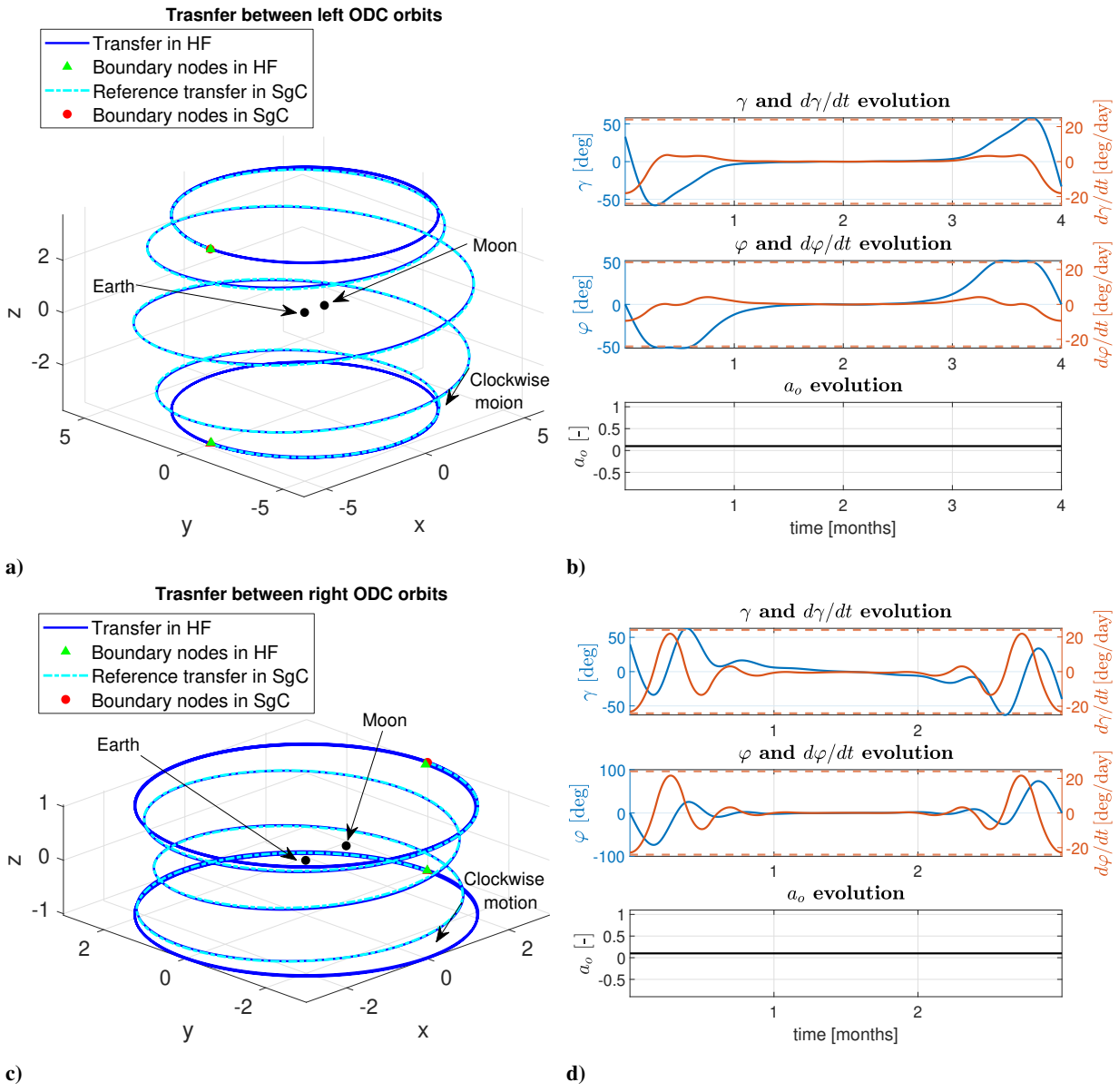

Fig. 15 Transfers between ODC orbits in the SgC (dahsed cyan) and HF (solid dark blue) frameworks and the required control histories: a-b) between the left ODC orbits, and c-d) between the right ODC orbits.

above and below the Earth-Moon (EM) orbital plane, respectively). All DC orbits employ a simple Sun-facing steering law in which the solar sail is tilted at a constant angle with respect to the direction of sunlight in the out-of-plane direction. The various DC orbits in the family are parametrized by this angle.

From each sub-family, two optimal distant-circular (ODC) orbits (northern and southern) have been selected. These ODC orbits are optimal in the sense that they have the best properties for polar observation of the Earth and Moon. Note that, due to the symmetry of the dynamics with respect to the orbital plane of the EM system, the following discussion, which focuses on the northern orbits and observation of the Earth and lunar north poles, is also valid for their southern

counterparts. One single sailcraft in the left northern ODC orbit is capable of providing continuous coverage of both the Earth and lunar north poles throughout the year at a minimum elevation of 14 deg with respect to the lunar north pole and at six EM distances for both north poles. For the right northern ODC orbit, continuous coverage of the Earth's north pole is not achieved, but the sailcraft would be closer to both poles at approximately three EM distances.

The ODC orbits have been migrated to a higher-fidelity dynamical framework, which includes perturbations by the eccentricity of the Moon's orbit, the offset between the plane of the EM system and the ecliptic, and the heliocentric eccentricity of the EM system's barycenter. The migration has been performed by means of a multiple-shooter differential corrector adapted to the non-autonomous property of the solar-sail EM three-body problem. Two types of migration have been considered: with and without active control. Both types of control allow seemingly quasi-periodic trajectories that remain bounded to the reference orbits without loss in the coverage capabilities. As a case study, we analyzed the control of the right southern ODC orbit over a time period of one year. We found that it is possible to maintain a bounded quasi-periodic trajectory with a maximum offset of 2560 km from the reference orbit for an increase of the reference sail's performance of 40 %.

Finally, transfer trajectories were developed between the northern and southern ODC orbits with transfer times of three to four months. These transfers allow a single sailcraft to observe both the northern and southern latitudes of the Earth and/or Moon during a single mission and as such may increase the mission scientific return.

References

[1] Tsuda, Y., Mori, O., Funase, R., Sawada, H., Yamamoto, T., Saiki, T., Endo, T., Yonekura, K., Hoshino, H., and Kawaguchi, J., "Achievement of IKAROS — Japanese Deep Space Solar Sail Demonstration Mission," *Acta Astronautica*, Vol. 82, No. 02, 2013, pp. 183–188. https://doi.org/10.1016/j.actaastro.2012.03.032.

[2] Johnson, L., Whorton, M., Heaton, A., Pinson, R., Laue, G., and Adams, C., "NanoSail-D: A Solar Sail Demonstration Mission," *Acta Astronautica*, Vol. 68, No. 5-6, 2011, pp. 571–575. https://doi.org/10.1016/j.actaastro.2010.02.008.

[3] Biddy, C., and Svitek, T., "LightSail-1 Solar Sail Design and Qualification," *Proceedings of the 41st Aerospace Mechanisms Symposium*, Jet Propulsion Laboratory, National Aeronautics and Space Administration Pasadena, CA, 2012, pp. 451–463.

[4] Betts, B., Spencer, D. A., Nye, B., Munakata, R., Bellardo, J. M., Wong, S. D., Diaz, A., Ridenoure, R. W., Plante, B. A., and Foley, J. D., "Lightsail 2: Controlled Solar Sailing Using a CubeSat," *The 4th International Symposium on Solar Sailing. Kyoto Research Park, Kyoto, Japan 17–20 Jan*, 2017.

[5] McNutt, L., Johnson, L., Kahn, P., Castillo-Rogez, J., and Frick, A., "Near-Earth Asteroid (NEA) scout," *AIAA Space 2014 Conference and Exposition*, American Institute of Aeronautics and Astronautics, San Diego, CA, USA, 2014, p. 4435. https://doi.org/10.2514/6.2014-4435.

[6] Pezent, J., Sood, R., Heaton, A., Miller, K., and Johnson, L., "Preliminary Trajectory Design for NASA's Solar Cruiser: A

Technology Demonstration Mission," *Acta Astronautica*, Vol. 183, 2021, pp. 134–140. https://doi.org/https://doi.org/10.1016/j.actaastro.2021.03.006.

[7] Macdonald, M., and McInnes, C. R., "Solar Sail Science Mission Applications and Advancement," *Advances in Space Research*, Vol. 48, No. 11, 2011, pp. 1702–1716. https://doi.org/10.1016/j.asr.2011.03.018.

[8] McInnes, C. R., *Solar Sailing: Technology, Dynamics and Mission Applications*, Springer-Praxis, 1999.

[9] Quarta, A. A., and Mengali, G., "Electric Sail Mission Analysis for Outer Solar System Exploration," *Journal of Guidance, Control, and Dynamics*, Vol. 33, No. 3, 2010, pp. 740–755. https://doi.org/https://doi.org/10.2514/1.47006.

[10] Dachwald, B., and Wie, B., "Solar Sail Kinetic Energy Impactor Trajectory Optimization for an Asteroid-Deflection Mission," *Journal of Spacecraft and Rockets*, Vol. 44, No. 4, 2007, pp. 755–764. https://doi.org/https://doi.org/10.2514/1.22586.

[11] Dachwald, B., Mengali, G., Quarta, A. A., and Macdonald, M., "Parametric Model and Optimal Control of Solar Sails With Optical Degradation," *Journal of Guidance, Control, and Dynamics*, Vol. 29, No. 5, 2006, pp. 1170–1178. https://doi.org/10.2514/1.20313.

[12] Heiligers, J., van den Oever, T. D., Ceriotti, M., Mulligan, P., and McInnes, C., "Continuous Planetary Polar Observation from Hybrid Pole-Sitters at Venus, Earth, and Mars," *The 4th International Symposium on Solar Sailing. Kyoto Research Park, Kyoto, Japan 17–20 Jan*, 2017.

[13] Heiligers, J., Vergaaij, M., and Ceriotti, M., "End-to-end trajectory design for a solar-sail-only pole-sitter at Venus, Earth, and Mars," *Fifth International Symposium on Solar Sailing*, Aachen, Germany, 2019. https://doi.org/10.1016/j.asr.2020.06.011.

[14] Heiligers, J., Macdonald, M., and S. Parker, J., "Extension of Earth-Moon Libration Point Orbits with Solar-Sail Propulsion," *Astrophysics and Space Sciences*, Vol. 361, 2016, p. 241. https://doi.org/10.1007/s10509-016-2783-3.

[15] Heiligers, J., Parker, J., and Macdonald, M., "Novel Solar Sail Mission Concepts for High-Latitude Earth and Lunar Observation," *Journal of Guidance, Control, and Dynamics*, Vol. 41, No. 01, 2018, pp. 212–230. https://doi.org/10.2514/1.g002919.

[16] Wawrzyniak, G. G., and Howell, K. C., "Generating Solar Sail Trajectories in the Earth-Moon System Using Augmented Finite-Difference Methods," *International Journal of Aerospace Engineering*, Vol. 2011, 2011. https://doi.org/10.1155/2011/476197.

[17] Ozimek, M. T., Grebow, D. J., and Howell, K. C., "Design of Solar Sail Trajectories With Applications to Lunar South Pole Coverage," *Journal of Guidance, Control, and Dynamics*, Vol. 32, No. 6, 2009, pp. 1884–1897. https://doi.org/10.2514/1.41963.

[18] Wakker, K. F., *Fundamentals of astrodynamics*, TU Delft Library, 2015.

[19] Szebehely, V., *Theory of Orbits. The Restricted Problem of Three Bodies*, Academic press. New York and London, 1967. https://doi.org/10.1119/1.1974535.

[20] Battin, R. H., *An Introduction to the Mathematics and Methods of Astrodynamics, Revised Edition*, American Institute of Aeronautics and Astronautics, Inc., 1999. https://doi.org/10.2514/4.861543.

[21] Heiligers, J., Diedrich, B., Derbes, W., and McInnes, C. R., "Sunjammer: Preliminary End-to-End Mission Design," *AIAA/AAS Astrodynamics Specialist Conference*, 2014, p. 4127. https://doi.org/10.2514/6.2014-4127.

[22] Dachwald, B., "Solar Sail Dynamics and Control," *Encyclopedia of Aerospace Engineering*, 2010. https://doi.org/10.1002/9780470686652.eae292.

[23] Heiligers, J., Guerrant, D., and Lawrence, D., "Exploring the Heliogyro's Orbital Control Capabilities for Solar Sail Halo Orbits," *Journal of Guidance, Control, and Dynamics*, Vol. 40, No. 01, 2017, pp. 1–18. https://doi.org/10.2514/1.g002184.

[24] Ma, D., Murray, J., and Munday, J. N., "Controllable Propulsion by Light: Steering a Solar Sail via Tunable Radiation Pressure," *Advanced Optical Materials*, Vol. 5, No. 4, 2017, p. 1600668. https://doi.org/https://doi.org/10.1002/adom.201600668.

[25] Gong, S., Li, J., and Simo, J., "Orbital Motions of a Solar Sail Around the L_2 Earth–Moon Libration Point," *Journal of Guidance, Control, and Dynamics*, Vol. 37, No. 4, 2014, pp. 1349–1356. https://doi.org/https://doi.org/10.2514/1.G000063.

[26] Miele, A., "Revisit of the Theorem of Image Trajectories in the Earth-Moon Space," *J. Optimization Theory and Applications*, Vol. 147, No. 12, 2010, pp. 483–490. https://doi.org/10.1007/s10957-010-9734-x.

[27] Grebow, D., "Generating Periodic Orbits in the Circular Restricted Three-Body Problem With Applications to Lunar South Pole Coverage," Master's thesis, School of Aeronautics and Astronautics, Purdue University, 2006.

[28] Boroson, D. M., and Robinson, B. S., "The Lunar Laser Communication Demonstration: NASA's First Step Toward Very High Data Rate Support of Science and Exploration Missions," *Space Science Reviews*, Vol. 185, No. 1-4, 2014, pp. 115–128. https://doi.org/https://doi.org/10.1007/s11214-014-0122-y.

[29] Ward, R. L., Fleddermann, R., Francis, S., Mow-Lowry, C., Wuchenich, D., Elliot, M., Gilles, F., Herding, M., Nicklaus, K., Brown, J., Burke, J., Dligatch, S., Farrant, D., Green, K., Seckold, J., Blundell, M., Brister, R., Smith, C., Danzmann, K., Heinzel, G., Schütze, D., Sheard, B. S., Klipstein, W., McClelland, D. E., and Shaddock, D. A., "The Design and Construction of a Prototype Lateral-Transfer Retro-Reflector for Inter-Satellite Laser Ranging," *Classical and Quantum Gravity*, Vol. 31, No. 9, 2014, p. 095015. https://doi.org/10.1088/0264-9381/31/9/095015.

[30] Sood, R., and Howell, K. C., "Solar Sail Transfers and Trajectory Design to Sun-Earth L_4, L_5: Solar Observations and Potential Earth Trojan Exploration," *The Journal of the Astronautical Sciences*, Vol. 66, 2019, p. 247–281. https://doi.org/10.1007/s40295-018-00141-4.

[31] Fernandez, A., Heiligers, J., and Heaton, A. F., "Solar Sail Transfers from Invariant Objects to L_5 Periodic Orbits," *7th International Conference on Astrodynamics Tools and Techniques, November*, 2018.

[32] Marchand, B. G., Howell, K. C., and Wilson, R. S., "Improved Corrections Process for Constrained Trajectory Design in the n-Body Problem," *Journal of Spacecraft and Rockets*, Vol. 44, No. 4, 2007, pp. 884–897. https://doi.org/10.2514/1.27205.

[33] McInnes, A. I. S., "Strategies for Solar Sail Mission Design in the Circular Restricted Three-Body Problem," Master's thesis, School of Aeronautics and Astronautics, Purdue University, 2000.

[34] Biggs, J., McInnes, C. R., and Waters, T., "Control of Solar Sail Periodic Orbits in the Elliptic Three-Body Problem," *Journal of Guidance Control and Dynamics*, Vol. 32, No. 01, 2009, pp. 318–320. https://doi.org/10.2514/1.38362.

[35] Hu, G., Ong, C., and Teo, C., "Direct Collocation and Nonlinear Programming for Optimal Control Problem Using an Enhanced Transcribing Scheme," *Proceedings of the 1999 IEEE International Symposium on Computer Aided Control System Design, Kohala Coast, HI, USA*, 1999, pp. 369–374. https://doi.org/10.1109/CACSD.1999.808613.

[36] Gámez Losada, F., "Controllability of Solar-Sail Orbits in the Earth-Moon System," Master's thesis, Delft University of Technology, 2019. URL http://resolver.tudelft.nl/uuid:3aa2c8bc-010d-4450-9ce7-04b0e2f40cfb.